J. Fluid Mech. (2010), *vol.* 654, *pp.* 99–139.
doi:10.1017/S0022112010000492

The influence of initial conditions on turbulent mixing due to Richtmyer–Meshkov instability†

B. THORNBER[1]‡, D. DRIKAKIS[1], D. L. YOUNGS[2] AND R. J. R. WILLIAMS[2]

[1]Fluid Mechanics and Computational Science Group, Aerospace Sciences Department, Cranfield University, Cranfield MK43 0AL, UK

[2]AWE, Aldermaston, Reading RG7 4PR, UK

(Received 5 August 2009; revised 25 January 2010; accepted 25 January 2010; first published online 12 May 2010)

This paper investigates the influence of different three-dimensional multi-mode initial conditions on the rate of growth of a mixing layer initiated via a Richtmyer–Meshkov instability through a series of well-controlled numerical experiments. Results are presented for large-eddy simulation of narrowband and broadband perturbations at grid resolutions up to 3×10^9 points using two completely different numerical methods, and comparisons are made with theory and experiment. It is shown that the mixing-layer growth is strongly dependent on initial conditions, the narrowband case giving a power-law exponent $\theta\approx0.26$ at low Atwood and $\theta\approx0.3$ at high Atwood numbers. The broadband case uses a perturbation power spectrum of the form $P(k)\propto k^{-2}$ with a proposed theoretical growth rate of $\theta=2/3$. The numerical results confirm this; however, they highlight the necessity of a very fine grid to capture an appropriately broad range of initial scales. In addition, an analysis of the kinetic energy decay rates, fluctuating kinetic energy spectra, plane-averaged volume fraction profiles and mixing parameters is presented for each case.

1. Introduction

This paper is concerned with the effects of initial conditions on the development of a turbulent mixing layer due to Richtmyer–Meshkov (RM) instability. This is related to the Rayleigh–Taylor (RT) instability, in that it involves the motion of a heavy and light fluid, driven in this case by an impulsive instead of continuous acceleration. The impulsive acceleration typically arises because of a shock wave, which passes from one fluid into the other. On the interface between the two fluids, there is usually a small perturbation, which could be surface roughness, a slightly non-planar shock, a machined perturbation, or an uneven fluid interface. The interaction between this perturbation and the incident shock wave seeds the fluid instability, which initially grows in a laminar, ordered manner. At late time, the ordered structures become turbulent, greatly enhancing the mixing of the two fluids.

This form of impulsive mixing is important in the understanding of many astrophysical phenomena, from supernovae to the dynamics of interstellar media. In the past few decades, it has been realized that the assumption of spherical symmetry in the simulations of supernovae is inadequate due to the growth of RM instabilities.

‡ Email address for correspondence: b.j.r.thornber@cranfield.ac.uk

Almgren *et al.* (2006) showed that the uneven shape of the supernova remnants is due in part to the combined influence of RM and RT instabilities acting on perturbations within the star before the supernova. Earth-bound phenomena include inertial confinement fusion (ICF), where a spherical capsule containing thermonuclear material is compressed using a powerful laser (Amendt *et al.* 2002). Once a critical level of compression has been reached, the fuel ignites and a burst of energy is released. In ICF, RM instability occurs at the interface between the light and heavy materials, triggering turbulent mixing. In this case, turbulent mixing has the dual effect of diluting and cooling the fuel, which reduces the efficiency of the reaction; hence, it is important that this mechanism is well understood. By contrast, in the field of supersonic combustion, RM mixing due to weak shocks improves the mixing between fuel and oxidizer, giving more efficient combustion.

A key observation regarding all of these applications is that experimental measurements (especially quantitative data) are very difficult, most notably in the cases of astrophysical flows and inertial confinement fusion. Thus, an understanding of the underlying flow physics relies to an unusual level on insights gained through modelling and numerical simulation. A number of studies have focused on the influence of initial conditions on the multi-mode RT instability (see e.g. Dimonte *et al.* 2004), and on the RM instability with an 'egg carton' two-mode initial condition (see e.g. Cohen *et al.* 2002 or Hill, Pantano & Pullin 2006). However, at present there are no published papers examining numerically this issue for the three-dimensional multi-mode RM instability; hence, this is the first time that detailed data on the flow phenomenology, growth rates, mixture parameters and turbulent kinetic energy spectra have been presented.

The current contribution investigates two specific initial conditions through numerical simulation. The first is an initial perturbation characterized by a constant power spectrum over a narrow band of high wavenumbers. This is employed to examine the growth of the RM instability at late times, or, equivalently, RM instability generated through shock interaction with a pre-developed turbulent mixing layer. Shock interaction with a narrowband combination of high-frequency modes triggers growth of a turbulent mixing layer purely via mode coupling of the high wavenumbers, when all significant modes within the system have saturated. Additionally, some experiments noted a dependence of the mixing-layer growth exponent on density ratio (Dimonte & Schneider 2000). This dependence has been investigated for two different density ratios, 3:1 and 20:1, to attempt to clarify this matter.

The second initial condition consists of a broadband linear combination of modes satisfying a power spectrum proportional to k^{-2}, where k is the wavenumber. This form of perturbation has practical importance as it is representative of the measured surface finish of an inertial confinement fusion capsule (Barnes *et al.* 2002). Previous numerical studies of the ablative RT instability by Dahlburg *et al.* (1995) have also employed this form of perturbation spectrum. If the initial conditions are forgotten then the asymptotic growth rate and associated statistics of the mixing layer should be the same as the narrowband case. However, as pointed out by Youngs (2004), it is possible that the combination of linear growth of the long wavelengths is faster than the growth of a turbulent mixing layer, hence dictating the overall growth of the mixing zone.

The aims of the current work are to determine which of the theoretical models is correct for a given initial condition, to provide empirical data for the calibration of lower order models (e.g. Reynolds-averaged Navier–Stokes methods) and to further the fundamental understanding of the instability. The layout of this paper is as follows.

In § 2, a brief summary of existing theory and experimental results for general multi-mode perturbations is presented. Section 3 describes the numerical methods employed, the effective resolution of the numerical methods and the sensitivity of results to the domain size. Section 4 details the results for the narrowband simulations at Atwood 0.5, § 5 examines high Atwood behaviour, followed by § 6, which examines the flow physics of the broadband initial condition at Atwood 0.5. Finally, § 7 summarizes the key results of the study.

2. Richtmyer–Meshkov flow physics

2.1. *Single-mode perturbations*

Richtmyer–Meshkov instabilities (Richtmyer 1960; Meshkov 1969) can be understood as the impulsive limit of the Rayleigh–Taylor instability, where the interface acceleration occurs impulsively as a result of a shock wave or a very rapid acceleration. This is often referred to as the baroclinic deposition of vorticity on the interface. The analysis considers flow at rest, with an initial sinusoidal perturbation between two fluids of density ρ_1 and ρ_2. It is assumed that the acceleration $g(t)$ is very large and occurs over a very short period of time (see e.g. Richtmyer 1960; Drazin & Reid 2004), giving

$$\frac{\mathrm{d}a}{\mathrm{d}t} = \mu k \Delta u a_0^+ A t^+, \tag{2.1}$$

where $At^+ = (\rho_2^+ - \rho_1^+)/(\rho_1^+ + \rho_2^+)$ is the Atwood number, the plus (+) indicates a post-shock quantity, and μ is a constant that is typically assumed to be 1 for weak shocks but can vary at high shock Mach numbers. Equation (2.1) is typically most accurate when the post-shock amplitude and densities are employed (Zhang & Sohn 1997). The post-shock amplitude can be computed by taking the initial amplitude and multiplying by the mean compression rate

$$\frac{(\rho_1 + \rho_2)^-}{(\rho_1 + \rho_2)^+}. \tag{2.2}$$

Equation (2.1) has been tested experimentally by Chapman & Jacobs (2006), Collins & Jacobs (2002) and Holmes *et al.* (1999) demonstrating good accuracy for linear growth up to $ka \approx 1$. At late time, the interface is composed of 'bubbles', where the lighter fluid penetrates into the heavier fluid and 'spikes', where the heavier fluid penetrates into the lighter fluid. The sinusoidal shape eventually becomes mushroom shaped at late times (large deformations).

A further understanding of the instability is gained by considering the flow to be incompressible, an approach that is applicable for the interaction of a fluid interface with a weak shock (Richtmyer 1960). The flow is assumed to be inviscid, irrotational and incompressible, hence can be defined by a velocity potential

$$\phi_{vel}(x, y) = S(x)\phi_0 \exp(-k\,|x|)\cos(ky), \qquad S(x) = \begin{cases} 1 & \text{if } x > 0, \\ -1 & \text{if } x < 0 \end{cases} \tag{2.3}$$

for a two-dimensional RM instability where the initial location of the mixing layer is at $x = 0$, where x is in the direction of shock propagation, y ranges from 0 to L and ϕ_0 is a parameter that controls the magnitude of the perturbation. For RM instability, the magnitude of the initial perturbation is determined from linear theory, giving $\phi_0 = At^+ \Delta u$. A key observation is that the deposition of vorticity at the interface

implies the presence of an irrotational flow field whose width is of the order of the wavelength of the perturbation.

2.2. *Multimode perturbations*

2.2.1. *Early time*

The models outlined in this section investigate the growth of a mixing layer where the perturbations have not yet become linearly saturated. This means that the short wavelengths can be nonlinear (turbulent), but that these can be overtaken by longer wavelengths growing at a slower but more persistent rate.

Dimonte, Frerking & Schneider (1995) showed that if the mixing-layer width is governed by the width of the 'just saturated' bubble, then the total width (envelope described by the saturated modes) should grow with $\theta = 1/2$. This was derived by assuming that the 'just saturated' mode has amplitude $a \approx C_{RM}/k$, i.e. $ka \approx C_{RM}$, where C_{RM} should be of the order 1. Given linear growth of each mode to this amplitude, the governing equation is $\mathrm{d}a/\mathrm{d}t = (At)k\Delta u a_0$. Substituting $k = C_{RM}/a$, $W = 2a$ and $W_0 = 2a_0$ then $\mathrm{d}(W^2)/\mathrm{d}t = 4C_{RM}(At)\Delta u W_0$, the solution of this equation is

$$W \approx \sqrt{W_0^2 + 4C_{RM}At W_0 \Delta u (t - t_0)}. \tag{2.4}$$

Youngs (2004) proposed a modification to the growth rate by including the effects of initial conditions. Assuming that the power spectrum of the initial perturbation is represented by $P(k) \propto Ck^m$, the mean amplitude as a function of wavelength $1/k$ in a band around k can be written as $a(1/k) \propto \sqrt{kP(k)} = C^{1/2}k^{(m+1)/2}$. For $m \leqslant -1$, the power spectrum will diverge at $k = 0$; hence, it is assumed that a finite problem of size L is being considered where the power spectrum is applicable for wavenumbers greater than $2\pi/L$. The velocity corresponding to each wavenumber is then $v(k) = C^{1/2}(At)\Delta u k^{(m+3)/2}$. A structure of size $1/k$ becomes nonlinear in time $t = 1/kv(k)$. Linking the width of the mixing layer W with the wavelength $\lambda = 1/k$ gives

$$W \approx \lambda \approx \left(C^{1/2}(At)\Delta u t\right)^{2/(m+5)}, \tag{2.5}$$

thus giving $\theta = 2/(m + 5)$. Youngs (2004) argues that growth from mode coupling alone is approximately $\theta = 0.24$; hence, if the linearized growth rate is faster than this ($m < 3.3$) then θ is dependent on initial conditions. An equivalent result has also been given by Inogamov (1999).

Inogamov (2006) proposed another variant based upon the expansion of the mixing layer due to linearly saturated modes, considering a power spectrum of the initial perturbations that becomes constant at low wavenumbers (long wavelengths). He then examines the random mean square deviations in velocity fluctuations using ideas from random walk, concluding that $W \propto t^{1/3}$. The amplitude of the Fourier harmonics of the perturbation must not change significantly in the region $\pm n$ from the mode number n.

2.2.2. *Late time*

Barenblatt, Looss & Joseph (1983) discussed the case of an isolated sheet of developing turbulence. This is equivalent to assuming that all perturbations present in the initial condition have gone past the initial linear stage of growth dictated by Richtmyer's formula (2.1) and become a fully turbulent mixing layer. If the flow is not deformed by a mean shear, then the evolution of turbulent kinetic energy $q_K = \overline{(u^2 + v^2 + w^2)}/2$ is governed by a balance of turbulent diffusion and dissipation into heat. Assuming a turbulent energy eddy diffusion coefficient K_q, then dimensional

analysis gives $K_q = L\sqrt{q}_K$, $\epsilon = bq_K^{3/2}/L$, where L is a reference length scale, which can be taken as $L = Ch(t)$, h is a measure of the width of the mixing zone and (b) is a positive coefficient. The asymptotic late-time solution for the growth of the slab gives $h(t) \propto t^{1-\nu}$, where $\nu \geqslant 1/3$. That θ should be asymptotically less than 2/3 can also be derived through kinetic energy conservation $KE = 1/2\rho u^2 h \propto \rho h^3/t^2$ giving $h \propto t^{2/3}$. This argument was further developed by Youngs (1994), who employed the following model equations:

$$\frac{\mathrm{d}(Lq_K)}{\mathrm{d}t} = -bu^3, \quad \frac{\mathrm{d}W}{\mathrm{d}t} = u, \quad \text{where } L = cW + \mathrm{d}\lambda_{min}, \tag{2.6}$$

where the reference length L is taken as the minimum perturbation length scale λ_{min} and (b), (c) and (d) are model constants. Taking initial conditions of $W = 0$ and $u = \Delta u$ then

$$\frac{W}{\lambda_{min}} = \frac{d}{c}\left[\left(1 + \frac{c\Delta u t}{\theta \mathrm{d}\lambda_{min}}\right)^{\theta} - 1\right], \tag{2.7}$$

where $\theta = 2/(3 + bc)$, again recovering $\theta = 2/3$ for the case of zero viscosity, but now including some influence of the initial conditions. This equation applies to the growth of a mixing layer where the kinetic energy is confined to the region of turbulent mixing, whereas (2.5) applies where most of the kinetic energy is present in the irrotational flow field outside the region of turbulent mixing (generated during shock interaction as described in § 2.1). Ramshaw (1998) also gained $\theta = 2/3$ when dissipation is zero via a Lagrangian description of the mixing-layer width.

Gauthier & Bonnet (1990) extended the established $k - \epsilon$ methodology to model shock tube experiments. An analysis of the diffusion term in the turbulent kinetic energy equation and assuming self-similar growth leads to a growth of the mixing layer proportional to $t^{1/3}$. Huang & Leonard (1994) proposed a new self-similar decay of homogeneous turbulence that was shown to give a growth rate of $t^{1/4}$ at late times where the Reynolds number is low (Prasad *et al.* 2000). Mikaelian (1989) used the impulsive limit of the RT instability within a model for developing turbulent kinetic energy, predicting that the mixing layer grows as $0.14\Delta u(At)t$ at late times.

Zhou (2001) has applied the theory developed for turbulent flows with an external agent to the RM instability. As RM turbulence is anisotropic in the z-direction (the direction of shock propagation), Zhou examined the two-dimensional spectra in the plane perpendicular to shock propagation, proposing

$$E(k) = C\,[(At)\Delta u \epsilon(z)]^{1/2}\, k^{-3/2}. \tag{2.8}$$

When the time scale for RM mixing is less than the time scale for homogeneous decaying turbulence then the spectra should take the form above, else the turbulence will become fully developed and revert to a Kolmogorov form. The growth rate of the mixing layer is predicted to be $\theta = 7/12$, when the low wavenumber end of the spectrum follows a power law proportional to k^4 and $\theta = 5/8$ for k^2. More recently, by analogy to weakly anisotropic turbulence, Clark & Zhou (2006) derived $2/7 < \theta \leqslant 2/5$.

Llor (2006) has examined the behaviour of a freely decaying slab of turbulence with respect to the invariance of angular momentum at the large scales, using the knowledge that given a low wavenumber range proportional to k^c, there exists an invariant of the form $I = k\lambda^{c+1}$. From this it can be shown that for self-similar decay, the kinetic energy $q_K \propto t^{-n}$ and $\lambda \propto t^{1-n/2}$, where $n = (2c + 2)/(c + 3)$ (i.e. $\theta = 1 - n/2$). Assuming a Saffman impulse field as initial conditions for the turbulent slab, this gave $n = 4/3$ hence $\theta = 1/3$. Llor (2006) also proposes a maximum decay rate of turbulent

kinetic energy of $n = 10/7$, corresponding to $\theta = 2/7$. Recently, Poujade & Peybernes (2010) have presented an analysis based on foliated turbulent spectra and foliated averages, predicting $1/4 \leqslant \theta \leqslant 2/7$.

Note that these analyses are typically applicable to moderate Atwood numbers where the growth exponent of the bubble and spike can be assumed to be close. As $At \to 1$, there is little or no shear force applied to the spike side of the interaction. This means that the initial linear growth is not slowed by interaction with the second fluid and hence possibly does not form a vortex or turbulent mixing layer, growing instead directly proportional to time. This high-Atwood-number limit is not considered in the models presented within this section.

2.3. *Experimental data*

Experimental results exhibit varying values of θ primarily due to what appears to be a strong dependence on initial conditions and inherent difficulties in extracting quantitative data. Dimonte & Schneider (1997) measure the growth rate at $At \approx 0.9$, for a Mach >10 shock. They determined the value of $\theta = 0.5 \pm 0.1$, higher than previous investigations, suggesting an Atwood number dependence on the growth rate. The initial conditions for the experiment consisted of a three-dimensional broadband perturbation on a machined surface; hence, the high value of θ is consistent with the theory for early time behaviour.

The dependence of the growth rate θ on the Atwood number was investigated in a linear electric motor experiment (Dimonte & Schneider 2000). The relationship between the bubble and spike growth rate was found to be

$$\theta_S = \theta_B \left(\frac{1 + At}{1 - At} \right)^{0.21 \pm 0.05} = \theta_B \left(\frac{\rho_2}{\rho_1} \right)^{0.21 \pm 0.05}, \quad \text{for } 0.15 \leqslant At \leqslant 0.96, \tag{2.9}$$

where $\theta_B = 0.25 \pm 0.05$. In this case, the experiments started with an initial RT unstable problem caused by the acceleration of the rig. The RM problem thus began with a nonlinear region of turbulent mixing with most of the kinetic energy at a dominant length scale, i.e. a narrowband case. The observation of two different values of θ for the spike and bubble also implies non-self-similar behaviour. One of the objectives of the high-Atwood-number case investigated in this paper is to investigate the potential causes of this departure from self-similarity.

In an assessment of the potential flow models, three-dimensional single-mode experiments at $At = 0.15$ conducted by Chapman & Jacobs (2006) show the best agreement with the potential models of Goncharov (2002) who stated $H_{b/s} = (2/(1 \pm At))/kt$. Oron *et al.* (2001) use a combination of three-dimensional simulation, a bubble competition model and a buoyancy-drag model to formulate scaling laws for the Rayleigh–Taylor and Richtmyer–Meshkov instabilities. For the Richtmyer–Meshkov instability in three dimensions, the models suggest $\theta_B \approx 0.2$–0.25 with both bubble and spike θ close to θ_B for $At < 0.5$ but predicts larger $\theta_{B,S}$ as At approaches unity. This implies the behaviour very similar to the experimental results of Dimonte & Schneider (2000).

Experiments in air and sulphur hexafluoride ($At \approx 0.67$) conducted by Prasad *et al.* (2000) examined the influence of initial conditions on the late-time growth of the turbulent mixing layer. The initial conditions were taken as a series of large-scale sinusoidal perturbations, broken by a high wavenumber component introduced via a wire mesh. There is a dependence of initial conditions, the largest wavelengths producing the thickest mixing layer; however, it is a weak dependence as the growth exponent over all experiments is $0.26 \leqslant \theta \leqslant 0.33$.

3. Numerical simulations

3.1. *Governing equations*

The computations presented here employ the Euler equations, where viscosity is assumed negligible ($Re \to \infty$). This involves solving in each principal direction the following governing equations:

$$\frac{\partial \boldsymbol{U}}{\partial t} + \frac{\partial \boldsymbol{E}}{\partial x} = 0, \tag{3.1}$$

where

$$\begin{aligned} \boldsymbol{U} &= [\rho,\ \ \rho u,\ \ \rho v,\ \ \rho w,\ \ \rho E,\ \ \rho\psi_1]^{\mathrm{T}}, \\ \boldsymbol{E} &= [\rho u,\ \ \rho u^2 + p,\ \ \rho uv,\ \ \rho uw,\ \ (\rho E + p)u,\ \ \rho u\psi_1]^{\mathrm{T}}, \\ \rho E &= \rho e + 0.5\rho\ (u^2 + v^2 + w^2), \end{aligned}$$

and ρ, (e), u, v, w, ψ_1 are the density, specific internal energy per unit volume, Cartesian velocity components and mass fraction of the heavy fluid. Throughout this paper, it is assumed that the fluid satisfies the ideal gas equation of state $p = \rho e\,(\gamma - 1)$, where $\gamma = 5/3$ is the ratio of specific heats and is identical for both fluids. The mass fraction equation is essentially a passive scalar that is advected to track the two gas components, assumed to be miscible. Before mixing, the two fluids are in pressure and temperature equilibrium i.e. the particle number densities, N_i, are the same. When mixing occurs it is assumed that pressure and temperature equilibrium occurs at small scales. For an analysis of the results, it is useful to define fluid volume fractions

$$f_i = \frac{N_i}{(N_1 + N_2)} = \frac{\dfrac{\psi_i}{M_i}}{\dfrac{\psi_1}{M_1} + \dfrac{\psi_2}{M_2}}, \tag{3.2}$$

where M_i is the molecular weight of fluid i and M_1/M_2 is identical to the initial density ratio. The use of volume fractions has advantages for diagnostic purposes. For example, if the post-shock mixing is incompressible (approximately true here) then $f_1 = (\rho - \rho_2)/(\rho_1 - \rho_2)$ and the mean volume fraction profile is equivalent to a scaled density profile.

3.2. *Numerical methods*

As neither of the numerical methods employ an explicit subgrid model, they fall in to the class of implicit large-eddy simulation (ILES) (Drikakis 2003; Grinstein, Margolin & Rider 2007; Drikakis *et al.* 2009). Conventional LES, where an explicit subgrid model is added to the averaged Navier–Stokes equations, has been employed successfully in many prototype flows; however, it is known to provide excessive dissipation in flows where the growth of an initially small perturbation to fully turbulent flow must be resolved (Lesieur & Metais 1996; Pope 2000). In addition, the construction of subgrid models appropriate for use in strongly compressible flows with high density gradients and shock waves is not straightforward.

It has been observed that for certain cases it is possible to construct numerical methods in which the subgrid dissipation is provided by the numerical method. This employs the Kolmogorov assumption of separation of scales – as long as the evolution of the large eddies of concern is independent of numerical viscosity, their evolution is captured accurately and is independent of the form of the viscosity employed. The critical design criteria for such schemes is that the dissipation of turbulent kinetic

energy provided by the large scales are isolated to the high wavenumbers that are anyway not resolved by the numerical method.

The behaviour at high wavenumbers should then remain localized, i.e. not cause a global instability due to excessively low or high total dissipation, and not influence the large eddies. This influence can manifest itself in two forms, either through the direct action of numerical dissipation or through secondary influence caused by a lack of or excess of eddies at high frequencies. An excess of eddy motion close to the cutoff will remove energy at a faster than physical rate from neighbouring eddies in wavenumber space, and a lack of high wavenumber eddies will remove energy from these eddies at a slower rate. Ideally, this dissipation rate would be controlled using explicit filtering satisfying the required dissipation rate (adapting the approach by Bogey, de Cacqueray & Bailly 2009 for example); however, this inevitably increases the thickness of the contact surface and shock (in terms of number of grid points) and suffers from the same difficulties as the classical subgrid modelling.

This paper approaches the problem of turbulence modelling through a systematic grid refinement study such that at the highest grid level it is reasonable to assume that there is sufficient separation between the dynamic and dissipative scales so that a physically realistic turbulent flow field is achieved. Thus, the large scales evolve independent of numerical viscosity, as is confirmed through an analysis of the kinetic energy spectra within this paper. The two numerical methods employed here are described in more detail in the following subsections.

3.2.1. *CNS3D*

CNS3D (Drikakis & Tsangaris 1993; Drikakis 2003; Thornber *et al.* 2008) solves the governing equations using a finite volume Godunov-type method (Godunov 1959; Drikakis & Rider 2004). The inter-cell numerical flux is computed based on the solution to the Riemann problem using the reconstructed variables at the left and right of the cell interface. In this paper, the Harten–Lax–van Leer contact (HLLC) approximate Riemann solver is employed as detailed by Toro (1997).

Higher-order accuracy is achieved using monotonic upwind scheme for conservation laws (MUSCL) extrapolation (van Leer 1977), with the fifth-order limiter proposed by Kim & Kim (2005) implemented in a one-dimensional form for a fast computational time. The standard MUSCL extrapolation has been augmented using the method of Thornber *et al.* (2008), which involves an additional stage in the reconstruction process for the velocity vector. It ensures a uniform dissipation of the kinetic energy in the limit of zero Mach number (M), extending the validity of the Godunov method to at least $M \approx 10^{-4}$, via a progressive central differencing of the velocity components. The formulation of the underlying governing equations is not changed, and monotonicity of the density and scalar field is maintained.

Thornber *et al.* (2008) showed that the leading-order kinetic energy dissipation rate is proportional to $u^3/\Delta x$ for the modified scheme, similar in form to that proposed by Kolmogorov (1941) for decaying turbulence. It is this dissipation rate that acts as a subgrid model in the ILES framework, giving a significantly improved high wavenumber performance compared with standard Godunov methods (Thornber, Mosedale & Drikakis 2007; Thornber & Drikakis 2008; Thornber *et al.* 2008).

Previously, numerical investigations have been performed for Richtmyer–Meshkov mixing using ninth-order weighted essentially non-oscillatory (WENO) methods (Mosedale & Drikakis 2007; Drikakis *et al.* 2009). However, when used in combination with the modified reconstruction method the scheme is not dissipative enough to employ as an ILES method, leading to significant turn-up at the high wavenumber end

of the energy spectrum in simulations of homogeneous decaying turbulence. Therefore, in the present study the fifth-order limiter was selected as a more computationally efficient and better-understood scheme for this type of flow.

Finally, a second-order accurate three-stage Runge–Kutta time-stepping method is employed (Spiteri & Ruuth 2002). This has an extended stability region to a theoretical CFL = 2, reducing computational time compared with other explicit methods.

3.2.2. *TURMOIL3D*

TURMOIL3D uses the Lagrange-remap method of Youngs (1982) extended to three-dimensional flows (Youngs 1991). The details of the algorithm will be summarized here; however, a more complete description is given in Chapter 4c of Grinstein *et al.* (2007). For turbulent mixing problems, a mass fraction advection equation is used for gas mixtures (Youngs 1991). The scheme is split into separate Lagrange and remap phases.

The Lagrange phase calculates the changes in velocity and internal energy due to the pressure field. A staggered mesh is used with velocity components defined at cell corners and with density, mass fraction and internal energy defined at cell centres. A finite-difference approximation is used which is second-order accurate in space and time, conserves total energy and is non-dissipative in the absence of shocks. Quadratic artificial viscous pressure q is used to provide the dissipation due to shocks. There are oscillations behind shocks. Hence, the treatment of shocks is not as good in some respects as in second-order Godunov methods. However, the method does have one very useful property: the irreversible dissipation of kinetic energy, $-q\nabla\cdot\boldsymbol{u}$, is negligible for low Mach number, near incompressible flow. This avoids the problem encountered in Godunov methods without the low Mach number correction of Thornber *et al.* (2008). All three spatial directions are calculated simultaneously in the Lagrange phase.

The remap phase calculates advective fluxes and may be regarded as a remap of the configuration at the end of the Lagrangian motion, back to the original mesh. The x, y and z advections are calculated in separate one-dimensional sweeps using a third-order monotonic method based on the work of van Leer. The order of the sweeps is reversed at every time step. The method gives an exact monotonic behaviour, i.e. fluid variables at the end of the remap phase lie with the range of neighbouring values at the end of the Lagrange phase. The remap phase conserves mass, internal energy and momentum. However, kinetic energy is dissipated. The loss of kinetic energy is quantified precisely as a function of position by the simple algebraic technique of Debar (1974) and may be added on to the internal energy to recover total energy conservation. This technique may be thought of as giving the 'subgrid dissipation'. In the remap phase, dissipation occurs where there are steep velocity gradients and is negligible in regions of smooth flow. It is comparable to that obtained with an explicit subgrid-scale model. Several Lagrange steps may be performed per remap step and this significantly increases the efficiency of low Mach number calculations.

CNS3D has been used to obtain most of the results. The alternative numerical technique (TURMOIL3D) used previously by Youngs (2004) has been employed to check key results and thereby increase confidence in the conclusions.

3.3. *Initialization*

The test case uses the initial conditions derived by Youngs (2004), which are shown schematically in figure 1. The flow field consists of a heavy and light gas separated by a perturbed interface where the perturbation satisfies a given power spectrum and

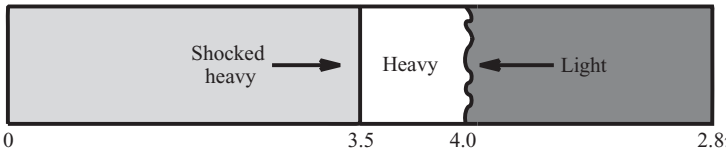

FIGURE 1. Schematic of the multi-mode Richtmyer–Meshkov initialization.

mean amplitude. The incident shock wave has a Mach number of 1.84, equivalent to a four-fold pressure increase. The initial conditions for CNS3D are

$$0.0 < x < 3.5 \quad (\rho, u, p) = (6.38, -6.15, 4000), \tag{3.3}$$

$$3.5 < x < 4.0 + \mathscr{S}(y, z) \quad (\rho, u, p) = (3.0, -29.16, 1000), \tag{3.4}$$

$$4.0 + \mathscr{S}(y, z) < x < L_D \quad (\rho, u, p) = (1.0, -29.16, 1000), \tag{3.5}$$

where $\mathscr{S}(y, z)$ is a two-dimensional array specifying the position of the interface in the x-direction. An initial velocity is given to the gas interface such that the centre of the interface is stationary after passage of the shock wave. The post-shock Atwood number $At^+ = 0.5$.

The accurate initialization of the surface perturbation $\mathscr{S}(y, z)$ requires careful consideration, as it is essential that the modes that form the initial perturbation are linear at initialization, so that Richtmyer's theory is applicable. This is relatively simple for the narrowband case, where the short wavelengths present in the initial perturbation have a top hat power spectrum between $\lambda_{min} = 16\Delta x$ and $\lambda_{max} = 32\Delta x$, where Δx is the mesh spacing. Specifying that the standard deviation of the surface perturbation should be $0.1\lambda_{min}$ ensures linearity.

For the broadband case the requirement of linearity of the highest wavenumbers leads to a more complex expression for the standard deviation, and for this reason the details are reproduced in Appendix A. The simulations using TURMOIL3D employed an equivalent velocity perturbation as initial condition, which is described in Appendix B. Visualizations of a slice and a three-dimensional perspective view of the initial condition for the broadband and narrowband perturbations are shown in figure 2.

Before proceeding further, it is important to justify the non-dimensionalizations used when presenting results in this paper. For a constant shock Mach number, the parameters influencing the growth of the mixing layer are At^+, Δu and λ_{min}. Using the theory in § 2.2.1, we obtain

$$\frac{W}{\lambda_{min}} \propto \left(At^+ \frac{\Delta u\,(t - t_0)}{\lambda_{min}} \right)^{2/3}. \tag{3.6}$$

To directly compare the simulations conducted on different grid resolutions, all length scales are normalized by the minimum wavelength λ_{min} and velocities by $(At^+)\Delta u$. Hence, the dimensionless time

$$\tau = t \frac{At^+ \Delta u}{\lambda_{min}}, \tag{3.7}$$

and the kinetic energy and kinetic energy spectra are scaled by $\lambda_{min}((At^+)\Delta u)^2\rho$, where $\rho = 1$.

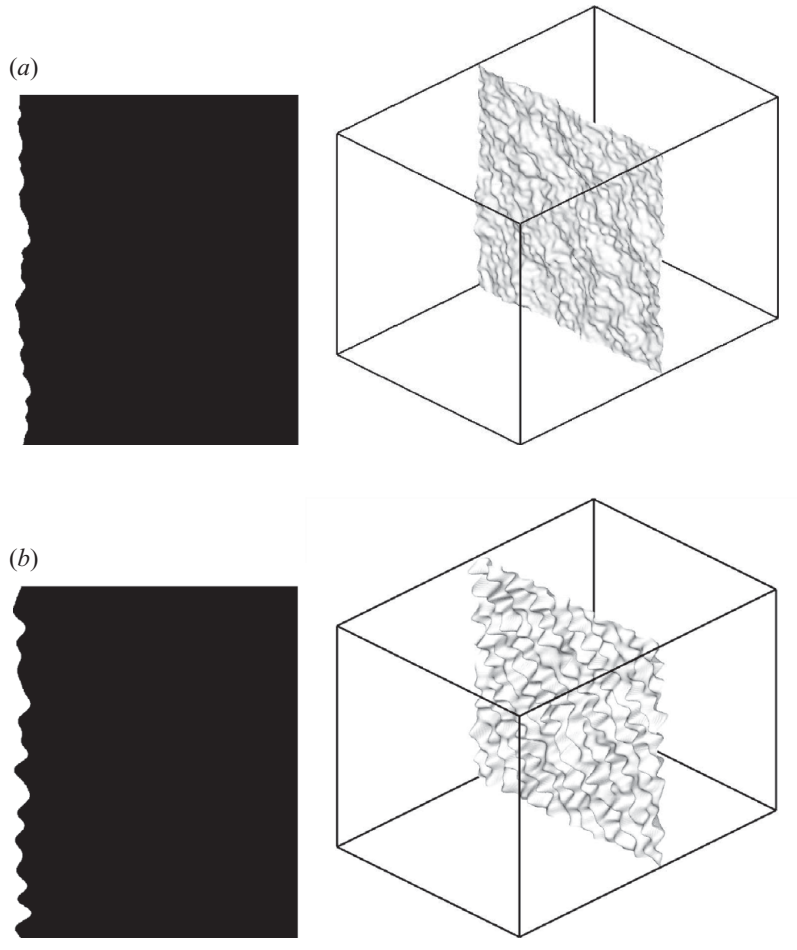

FIGURE 2. Illustration of the initial (*a*) broadband and (*b*) narrowband perturbations at 256 cross-section resolution, where the perturbation amplitude has been increased threefold to aid visualization.

The following paragraphs detail simulations undertaken to ensure that the chosen initial conditions for the broadband case are well resolved with the given numerical methods on the chosen grid sizes. Ideally, the broadband simulation will contain as wide a range of wavelengths as possible in the initial perturbation. However, it is clear that above a certain frequency the numerical method itself will influence significantly the solution obtained, and below a certain frequency there will be effects due to domain size and poor statistics.

The influence of the ratio of the smallest and largest wavelengths can be illustrated by considering linear theory developed in the previous section. The saturation times at one grid level (t_2) can be estimated from that at the previous level (t_1). Assuming that the mixing layer saturates when $W = c_{lmx}\lambda_{max}$, at two different resolutions labelled by subscripts 1 and 2 the ratio between the saturation times can be estimated using (3.6) as

$$\frac{t_1 - t_{1,0}}{t_2 - t_{2,0}} = R_{\lambda_{max}}^{3/2} R_{\lambda_{min}}^{-1/2}, \quad R_{\lambda_{max}} = \frac{\lambda_{max,1}}{\lambda_{max,2}}, \quad R_{\lambda_{min}} = \frac{\lambda_{min,1}}{\lambda_{min,2}}. \tag{3.8}$$

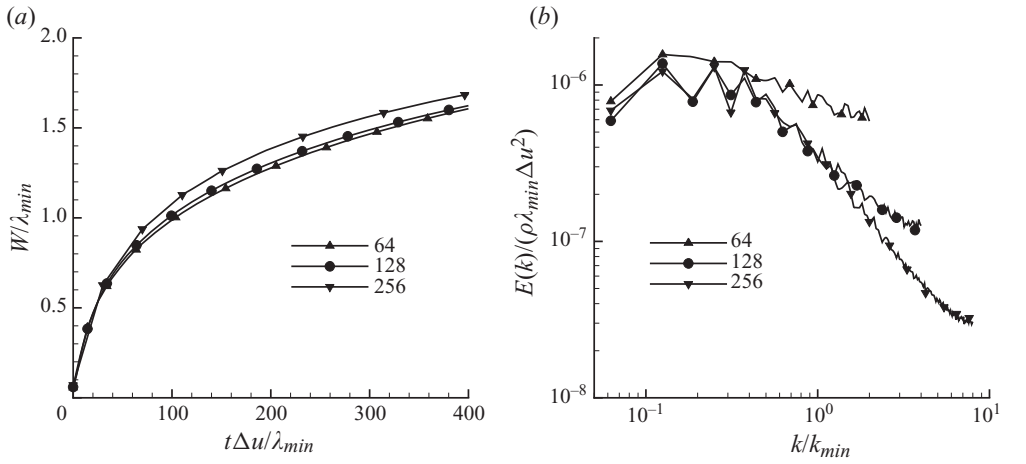

FIGURE 3. Grid convergence of (*a*) the integral mixing width and (*b*) the fluctuating kinetic energy spectra for CNS3D, where the grid levels are labelled by their respective cross-sectional resolution.

In a typical simulation, the longest wavelength remains constant as the mesh is refined, but the shortest wavelength is chosen as a function of the mesh spacing. This means that for each doubling of the mesh size, the dimensionless saturation time of the longest wavelength increases by a factor of $\sqrt{2}$. It is very important to maximize the ratio of the smallest to the largest wavelengths simulated to gain a longer period in which self-similar growth can develop.

Initial simulations were run to determine λ_{min} where modes excited are restricted between $\lambda_{min} = 32\pi/256$ and $\lambda_{max} = 2\pi/3$ on grid sizes of $360\times256\times256$, $180\times128\times128$ and $90 \times 64 \times 64$, with the domain size fixed at $2.8\pi \times 2\pi \times 2\pi$. This is essentially a convergence study with the same initial condition on all grids, only more poorly resolved on the coarsest grid. The time evolution of integral mixing width W, defined as

$$W = \int_0^{L_x} \langle f_1 \rangle \langle f_2 \rangle \, \mathrm{d}x, \tag{3.9}$$

is plotted in figure 3(*a*) for each of the cross-sectional resolutions. At 64 cross-section, the shortest wavelength spans only four grid points; hence, the behaviour at this resolution is dependent on the numerical method. The method employed here (CNS3D) gives a slightly faster growth than the converged solution. At 128 and 256 cross-sections, the growth rate appears to have converged, and at the final time the integral widths differ by less than 1.5 %.

The instantaneous two-dimensional kinetic energy spectra are plotted in figure 3(*b*), computed in the midplane of the mixing layer, in the y–z plane. A comparison between the different grids and methods shows that the method is not sufficiently dissipative at low resolutions (i.e. high wavenumbers). At the highest resolutions, there is excellent agreement for the first 48 modes when comparing the 128 and 256 cross-section grids, indicating that a good level of convergence has been achieved for the large scales, which is crucial for LES. From these simulations, it can be concluded that when $\lambda_{min} = 4\Delta x$, the initial perturbation is underresolved; however, when $\lambda_{min} \geqslant 8\Delta x$, the resulting growth is well resolved. For this reason, all broadband simulations within this paper use $\lambda_{min} = 8\Delta x$.

λ_{max}	N_x	$N_y = N_z$	$\lambda_{max}/\lambda_{min}$
$L/3$	90	64	$8/3 \approx 2.7$
$L/3$	180	128	$16/3 \approx 5.3$
$L/3$	360	256	$32/3 \approx 10.7$
$L/3$	720	512	$64/3 \approx 21.3$
$L/3$	1440	1024	$128/3 \approx 42.7$
$L/2$	90	64	4
$L/2$	180	128	8
$L/2$	360	256	16
$L/2$	720	512	32
$L/2^*$	360	1024	64
$L/2^*$	720	2048	128

TABLE 1. Grid sizes employed to determine the choice of λ_{max}. The asterisk (*) indicates reduced domain length.

The next parameter to fix is the size of the longest wavelength in the broadband case. In previous work, Youngs (2004) chose $\lambda_{max} = 2\pi/k_{min} = L/3$, where L is the box width. Simulations with $\lambda_{max} = L/2$ have also been run to maximize the range between the longest and shortest wavelengths. According to (3.8), the longer wavelength would give linear growth for a period ≈ 1.8 times longer at each grid level by extending the width of the perturbation range simulated. Table 1 details the grid sizes and λ_{max} employed in this study, where the domain size is $2.8\pi \times 2\pi \times 2\pi$, except at the highest resolution where a 'pancake' slice domain of size $0.7\pi \times 2\pi \times 2\pi$ was employed. Following this series of simulations, it was concluded that simulations with $\lambda_{max} = L/2$ were more efficient at a given grid level, and did not show any influence of domain size over the time scales considered.

The effect of different sets of random numbers to define the initial perturbation has been investigated via three simulations at 256 cross-sectional resolution using different random number sets. There is a maximum variation in the results at late time of $\pm 5\,\%$ due to the lack of modes at low wavenumbers, but the early time behaviour is nearly identical for all simulations. A comparison with the 1024 cross-section simulation demonstrates that the choice of random numbers does not affect the simulation significantly over the period of time in which the mixing layer is not affected by the largest scales.

The final important parameter to verify is the influence of the choice of domain size. To verify that the chosen domain size is adequate, additional simulations using twice the width and length of the 64 and 128 cross-section domain have been run. These simulations have employed the same λ_{max} and λ_{min} and grid spacing (i.e. same problem, double the domain size). When the growth is dominated by the evolution of the modes from linear to early nonlinear (marked by a good agreement with the high-resolution simulation), there is less than 1 % difference when the domain size is doubled. At late times, where the power in the large scales becomes important, the simulations vary by less than 5 %.

The domain size can be reduced at higher grid resolutions to take into account the fact that the simulations are run for a smaller physical time and grow at a slower rate. At the latest time for the 1024 cross-section simulation, the mixing layer extends to ± 0.5 from the mixing-layer centre. Given that the total domain size extends $\pm 1.4\pi$ from the centre of the mixing layer, there is substantial scope for reduction in computational effort. The consequence of a reduction in domain length is that the

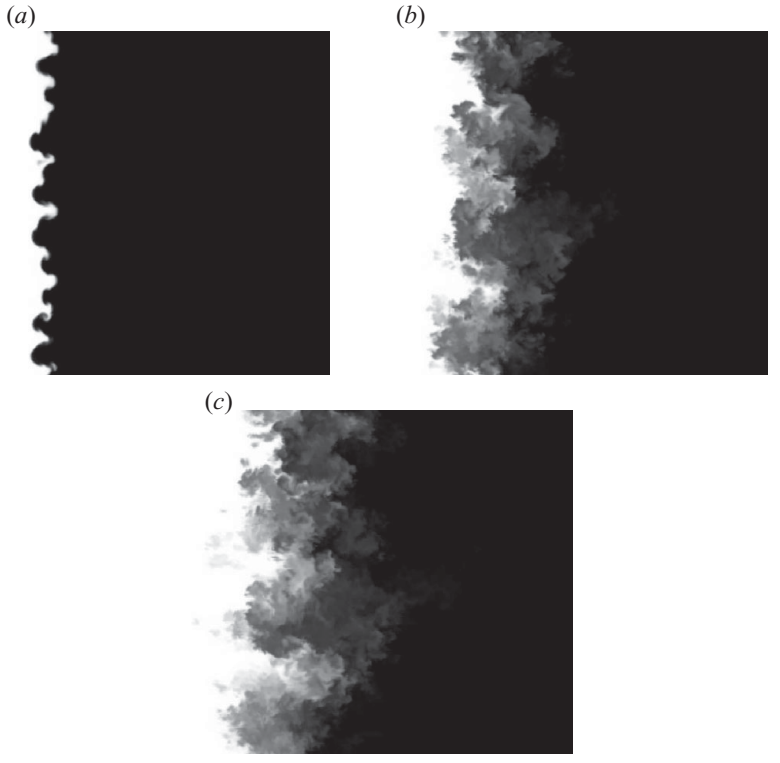

FIGURE 4. Two-dimensional visualizations of the evolution of the volume fraction for the $At^{+} = 0.5$ narrowband perturbations at $\tau = 3.7$, 111 and 260 using CNS3D at $360 \times 256 \times 256$ resolution.

influence of far-field fluid motion (i.e. slip surfaces generated as the curved shock leaving the interface becomes planar once more) is removed. It has been found that reducing the total domain length to 0.7π in simulations above 512 cross-section has no noticeable effect on the development of the mixing layer up to the point where the longest wavelengths are saturated. The reduction in computational time made a very high-resolution 2048 cross-section simulation feasible with the available resources.

4. Narrowband initial conditions at Atwood 0.5

4.1. *Flow phenomenology*

Figure 4 shows a two-dimensional slice through the flow field at three different time instants where a pure heavy fluid is white and pure light fluid is black. The shock initially travels from left to right; hence, the spikes move from left to right, the bubbles from right to left. Figure 5 shows volume fraction isosurfaces illustrating the evolution of the turbulent interface with time. Finally, figure 6 plots a three-dimensional view of the vortices, visualized as isosurfaces of 'Q' criterion (Jeong & Hussain 1995) where

$$Q = -\frac{1}{2}\frac{\partial u_i}{\partial x_j}\frac{\partial u_j}{\partial x_i}. \tag{4.1}$$

It can be seen that for early time ($\tau = 3.7$) the flow field consists of a series of mushroom-like structures generated by the deposition of vorticity at the gas interface. Each mushroom structure consists of a coherent vortex ring at early times, as can be

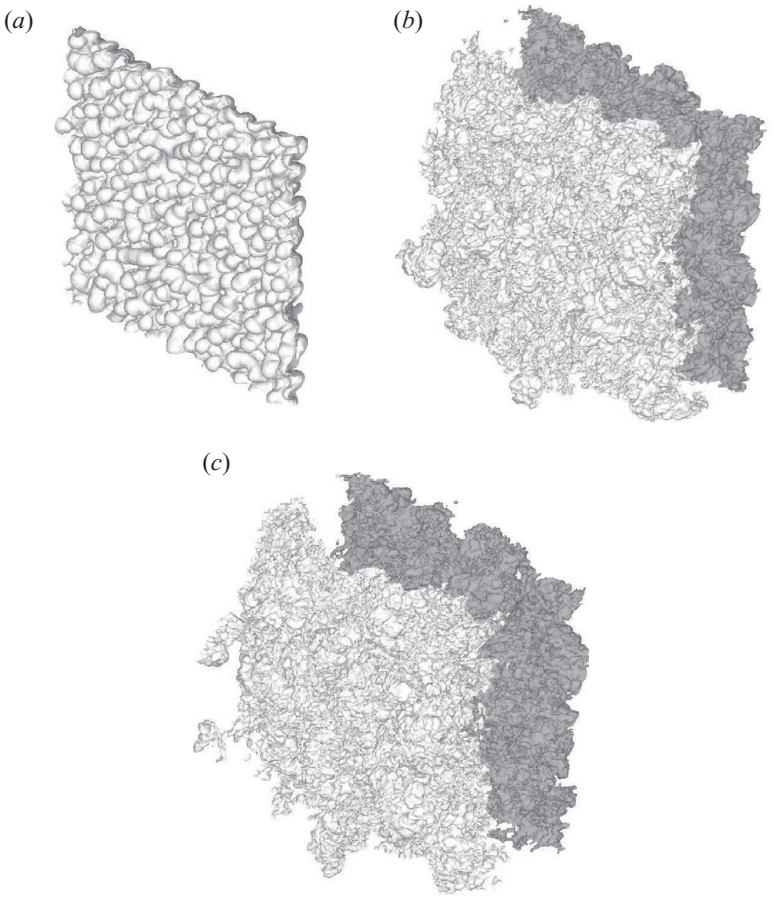

FIGURE 5. Isosurfaces of volume fractions 0.99 and 0.01 for the $At^+ = 0.5$ narrowband perturbations at $\tau = 3.7$, 111 and 260 using CNS3D at $360 \times 256 \times 256$ resolution.

clearly seen in figure 6. However, Kelvin–Helmholtz instabilities grow exponentially and break the coherent vortex rings at late time. The linear impulse given to certain modes allows them to escape the mixing zones before interaction with neighbouring vortices causes them to lose coherence; hence, small parcels of heavy fluid are carried a relatively long distance into the lighter fluid. At late time, the mixing layer is fully turbulent and vorticity is concentrated in small worm-like vortex structures typically seen in simulations of turbulent flow fields (see e.g. Vincent & Meneguzzi 1991 or Thornber & Drikakis 2007). At the latest time it can be seen that the single vortex rings that advect heavy material into the light have broken down into a 'bundle' of vortex tubes that continue to advect into the light material, albeit at a reduced velocity.

4.2. *Flow physics*

The integral width, defined in (3.9), has been computed for grid resolutions 64^3–512^3 and is shown in figure 7. There is excellent collapse of the integral width under the chosen scaling for resolutions of above 64^3, the higher resolutions allowing examination of a later time behaviour. A line of best fit is plotted, which was generated assuming a functional relationship of the form $W = A(t - t_0)^\theta$ using two methods. The first method used the nonlinear regression package in Mathematica to optimize the values of A, t_0 and θ to reduce the mean square difference. The second method

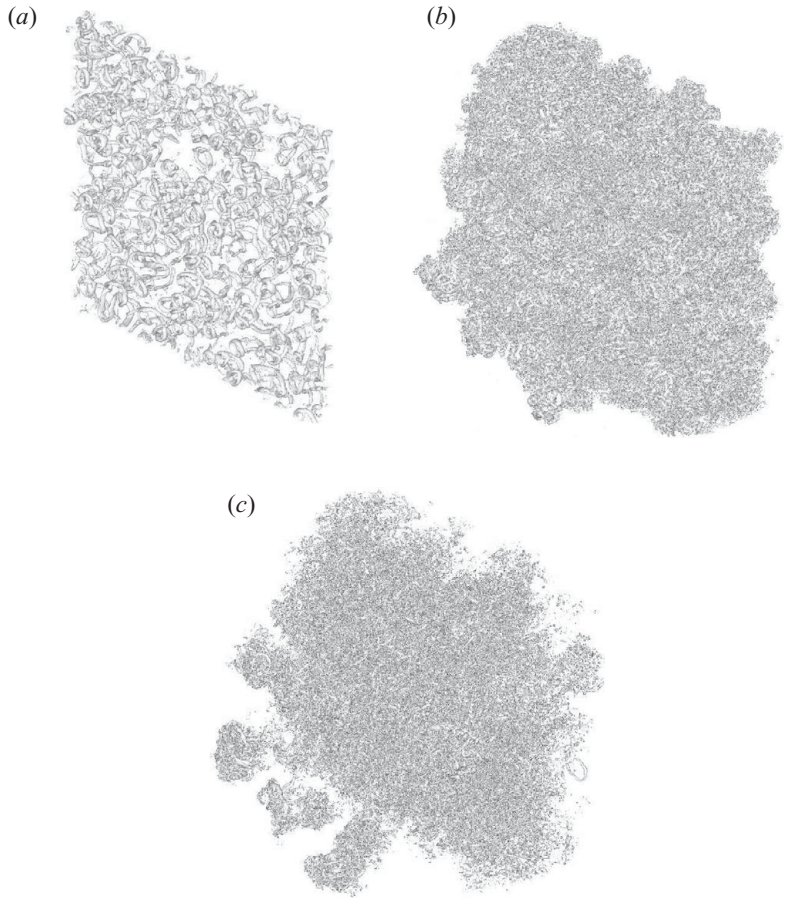

FIGURE 6. Visualization of vortex cores using $Q = 500$ at early time, $Q = 5$ for the two later times for the $At^+ = 0.5$ narrowband perturbations at $\tau = 3.7$, 111 and 260 using CNS3D at $360 \times 256 \times 256$ resolution.

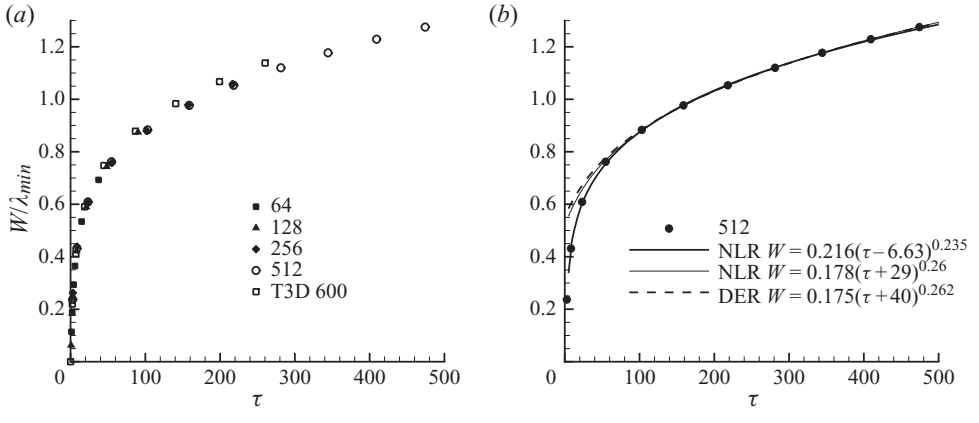

FIGURE 7. Variation of integral width with respect to grid resolution for the $At^+ = 0.5$ narrowband initialization (*a*) and with lines of best fit (*b*). 'DER' indicates fit calculated using derivatives of W and 'NLR' stands for nonlinear regression.

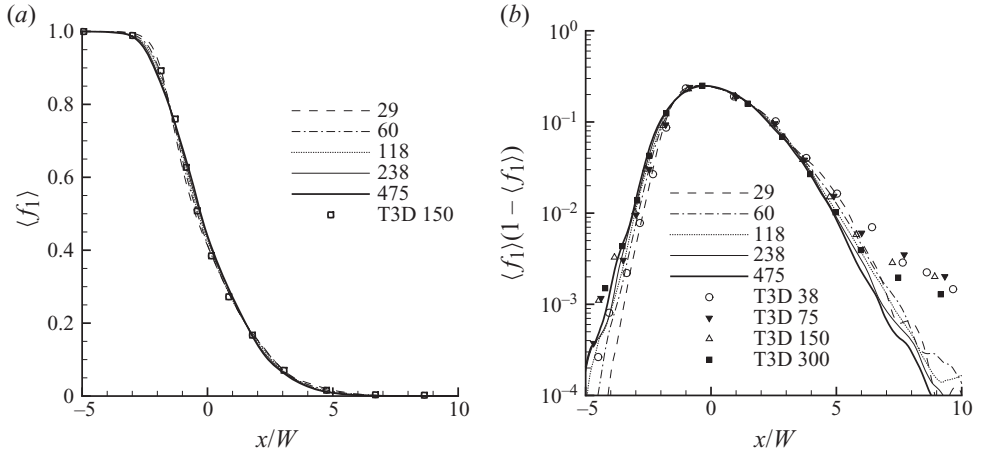

FIGURE 8. Profiles of (*a*) plane-averaged volume fractions $\langle f_1 \rangle$ of species one and (*b*) $\langle f_1 \rangle(1 - \langle f_1 \rangle)$ plotted against normalized distance for the 512 cross-section $At^+ = 0.5$ narrowband simulation at different dimensionless times.

calculates the data fit parameters using derivatives of the integral width, so that

$$\theta = \left(1 - \frac{W\ddot{W}}{\dot{W}^2}\right)^{-1}, \quad t_0 = t - \frac{(\theta - 1)}{\ddot{W}}\dot{W}, \quad A = \dot{W}\frac{(t - t_0)^{1-\theta}}{\theta}, \tag{4.2}$$

where the time derivatives $\dot{W}$ and $\ddot{W}$ were estimated to a second-order accuracy. This is similar to a previous approach used to estimate α in Rayleigh–Taylor instability (Ramaprabu 2003).

The nonlinear regression method using all points gave $A = 0.254$, $t_0 = 6.63$ and $\theta = 0.235$. Results fitted from $\tau = 20$ for TURMOIL3D give the same value of $\theta \approx 0.235$. Further analysis (presented later in this section) implies that self-similarity is not achieved until after $\tau = 40$. Using nonlinear regression on all points after $\tau = 40$ gave $A = 0.209$, $t_0 = -40$ and $\theta = 0.262$, where θ only varies by ± 0.002 if the nonlinear regression is chosen to begin anywhere between $\tau = 40$ and 500. The TURMOIL3D results are slightly lower, giving $A = 0.27$, $t_0 = -17$ and $\theta = 0.255$ for data fits after $\tau = 150$. Using the derivatives of the integral width, $A = 0.213 \pm 0.05$, $t_0 = 29. \pm 10$, $\theta = 0.26 \pm 0.02$. The uncertainty in the predictions using the derivatives is due solely to the evolution of the mixing layer – this is not necessarily perfectly smooth; hence, the variations in time of the results. The determination of t_0 is particularly sensitive to this.

These estimations are plotted in figure 7, showing excellent agreement over the range simulated. The lowest value of θ predicted fits well at early times, but at late times it begins to move below the simulation. A value of $\theta = 0.26$ matches the results closely, and is in good agreement with the experiments of Dimonte & Schneider (2000), who measured $\theta = 0.25 \pm 0.05$ for an impulsively driven instability, and the earlier simulations of Youngs (2004), who gained $\theta = 0.243$ (data fit from early time). Compared to analytical theory, this result is consistent with the general consensus that $\theta = 2/3 - \nu$ by Barenblatt *et al.* (1983), where the viscous correction $\nu \approx 0.41$ in this case, and in agreement with several of the analyses presented in § 2.2.2 (Prasad *et al.* 2000; Clark & Zhou 2006; Llor 2006; Poujade & Peybernes 2010). However, it is considerably lower than the lowest growth rate proposed by Zhou (2001).

Figure 8 shows the plane-averaged volume fraction profiles at several different times during the development of the mixing layer and a plot of $\langle f_1 \rangle(1 - \langle f_1 \rangle)$ to highlight the

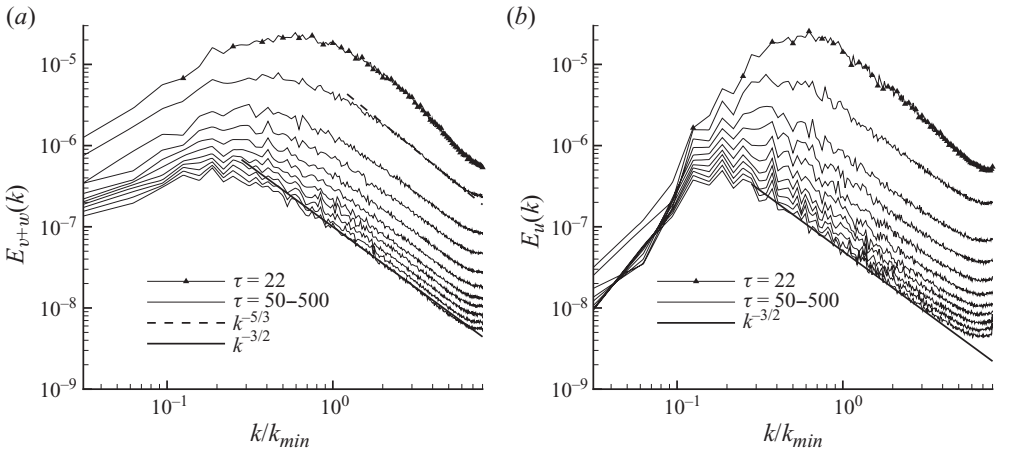

FIGURE 9. Fluctuating radial kinetic energy spectra for the 512 cross-section $At^+ = 0.5$ narrowband simulation at $\tau = 22$ and then from $\tau = 50$ to 500 in intervals of 50 for (a) the $v + w$ components and (b) the u component.

variation at the extremes of the layer. The profiles are self-similar after $\tau \approx 238$ in the bulk of the mixing layer. However, at the extremes of the mixing layer, self-similarity is achieved up to $\langle f_1 \rangle (1 - \langle f_1 \rangle) = 10^{-2}$, at which point there are visible differences between the two final times shown in figure 8 (although there is a factor of two difference in time). At time $\tau = 360$ (not shown for clarity), the plane-averaged volume fraction profile follows the $\tau = 475$ results up to $\langle f_1 \rangle (1 - \langle f_1 \rangle) = 10^{-3}$, demonstrating that a self-similar behaviour of the spikes is being approached, only more slowly than the bulk of the mixing layer. This is because there are two mechanisms for the growth of the mixing layer: the first is the growth of the fully developed turbulent 'slab' and the second is growth due to the linear momentum of the spike (vortex ring).

At $\tau = 475$, the spikes have not yet settled down to a self-similar behaviour, giving a discrepancy at $x/W \approx 5$ when compared to the fully self-similar profiles. At late times, the behaviour of the spikes themselves also becomes self-similar as shown by the collapse of the last five profiles in figure 8. The behaviour of the spikes is noticeably different between CNS3D and TURMOIL3D. The spikes in the former algorithm are less coherent and break down more rapidly, through a combination of Kelvin–Helmholtz and Widnall instabilities. This is because there is less dissipation at high wavenumbers in CNS3D compared to TURMOIL3D. As discussed below, in CNS3D there is an insufficient dissipation at high wavenumbers. This leads to the discrepancy between the two methods for $x/W > 5$ at late times, where TURMOIL3D predicts a higher plane-averaged mixing fraction. Much higher resolution simulations are required to calculate the extremities of the spikes reliably; however, a very little heavy fluid is involved in this part of the flow.

The fluctuating kinetic energy spectra are shown in figure 9 for the 512 cross-section resolution at several time instants. At early times the spectrum is peaked around the highest perturbation frequency k_{max}. By $\tau = 50$, a $k^{-5/3}$ inertial range appears (possibly only a transient towards a steady state spectrum); however, at later times a clear $k^{-3/2}$ range can be seen from $\tau = 100$ to $\tau = 500$. The peak of the kinetic energy spectrum moves progressively from $k/k_{max} = 1$ at the start of the simulation to $k/k_{max} = 0.2$ ($k \approx 7$) by the end, as expected from a decaying turbulent flow field. Ideally, there

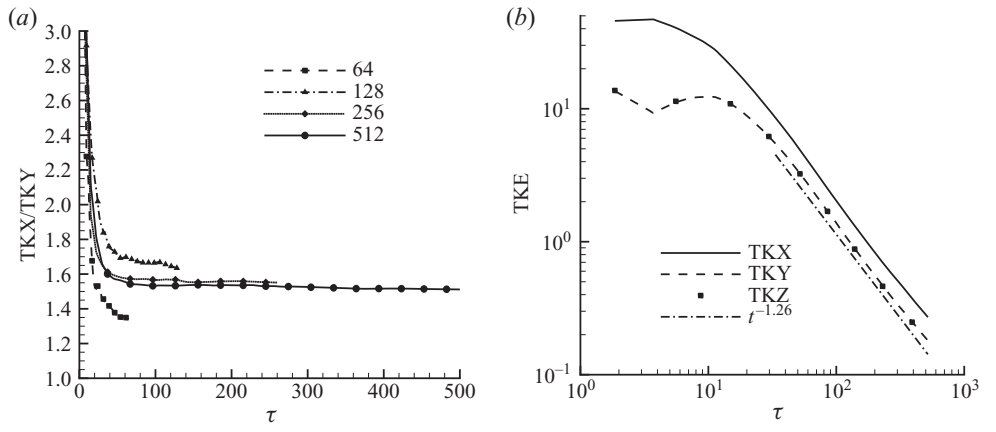

FIGURE 10. Plot of (*a*) ratio of fluctuating kinetic energies and (*b*) plot of *x*-, *y*- and *z*-directions total kinetic energy for the 512 cross-section $At^+ = 0.5$ narrowband simulation.

would be at least an order of magnitude of modes simulated below the peak of the kinetic energy spectrum; however, at the final time step, the most kinetic energy is in eddies 1/7th the domain size.

There is a clear difference in the behaviour of the velocities in the shock direction as compared with the transverse velocities. The spectrum of the u velocity (in the homogeneous direction) shows a $k^{-3/2}$ behaviour and the low wavenumber portion of the spectrum drops off more sharply than the transverse spectrum. The narrow width of the mixing layer compared with that of the box should imply that there is little energy in the velocities at the low wavenumbers (scales on the order of the box width); however, there is significantly more energy in the transverse directions than in the parallel directions at low wavenumbers below the driving scale. Similar anisotropy has been reported in the recent direct numerical simulation of a Rayleigh–Taylor instability by Cook, Cabot & Miller (2004).

As the subgrid model is implicit, the dissipation rate of turbulent kinetic energy is not 'designed' towards a particular form of sub-inertial range; hence, it is interesting that such a clear $k^{-3/2}$ range appears. At high wavenumbers, it is clear that there is not sufficient numerical dissipation ($k/k_{max} > 6.5$); however, it is unrealistic to expect any numerical method to resolve accurately to that high a wavenumber – an LES simulation of these fine scales would be prohibitively expensive.

Initially, it is expected that the RM mixing zone has double the kinetic energy in the x-direction than that in the y- and z-directions, as can be seen by computing the velocity components from the velocity potential in (B 1). To investigate this, the fluctuating velocities have been computed as the difference of the actual velocities minus the plane-averaged velocity, summed over the entire mixing layer, i.e.

$$\tilde{u} = \frac{\sum_{yz} \rho u \, \mathrm{d}V}{\sum_{yz} \rho \, \mathrm{d}V}, \quad TKX = \sum_{xyz} \frac{1}{2} \rho (u - \tilde{u})^2 \, \mathrm{d}V, \quad TKY = \sum_{xyz} \frac{1}{2} \rho v^2 \, \mathrm{d}V. \tag{4.3}$$

Figure 10 shows that in the simulations the initial anisotropies are higher as the shock is non-planar and contributes to the fluctuating kinetic energy in the x-direction. Zhou (2001) argued that at late time, a $k^{-5/3}$ sub-inertial range should develop and the mixing layer should become a slab of homogeneous decaying turbulence. However, there is evidence that the velocity components do not equilibrate – instead the ratio

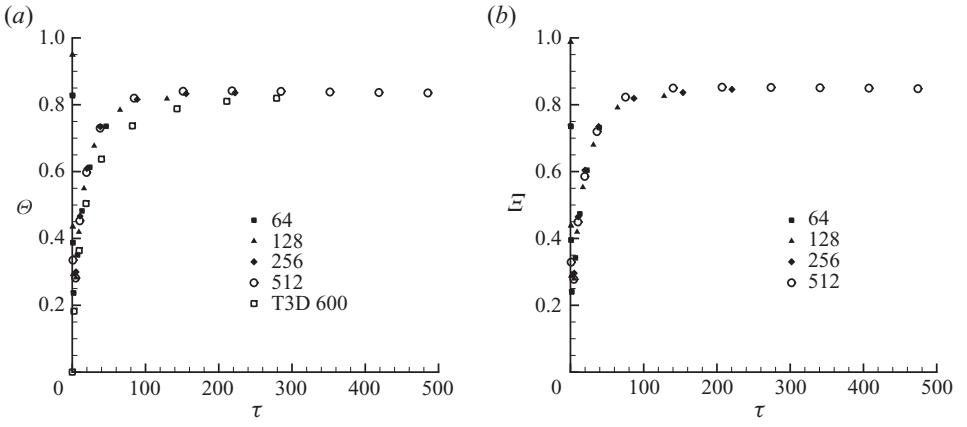

FIGURE 11. Molecular mixing parameters (*a*) Θ and (*b*) Ξ for the $At^+ = 0.5$ narrowband perturbation at different grid resolutions.

of the x-direction turbulent kinetic energy to the y-direction turbulent kinetic energy tends towards a constant value. Indeed, a self-similar decay of the mixing layer requires that the decay rate of the three velocity components is the same. This is shown clearly in figure 10 for the 512 cross-section, where the ratio of the x- and y-directions turbulent kinetic energy remains at 1.52 ± 0.02 for $200 \leqslant \tau \leqslant 500$. Given that this level of anisotropy exists, it is perhaps not surprising that $k^{-3/2}$ persists until late times. This indicates that the theories based on the assumption that at late time the mixing layer becomes a homogeneous isotropic turbulent slab may not be applicable to RM mixing.

Given that the width of the mixing layer scales with t^θ, the empirical relation $\epsilon \propto u^3/W$ can be used to check the dissipation rate of kinetic energy. From a dimensional analysis $\mathrm{d}q_K/\mathrm{d}t \propto q_K^{3/2}/t^\theta$, with a solution of the form $q_K \propto t^{2\theta-2}$. This is the decay rate of the mean kinetic energy across the mixing layer. The decay of total fluctuating kinetic energy shown in figure 10 (see (4.3)) is proportional to the width of the mixing layer multiplied by the mean kinetic energy, i.e. $Wq_K \propto t^\theta t^{2\theta-2} \propto t^{3\theta-2}$. This result can also be gained by assuming that the mean velocity in the mixing layer is proportional to the growth of the mixing layer itself, giving $\sqrt{q_k} \propto \mathrm{d}W/\mathrm{d}t \propto t^{\theta-1}$. Using $\theta = 0.26$, the decay of total fluctuating kinetic energy should be proportional to $t^{-1.22\pm0.06}$, within the margins of accuracy for the simulation that gave a decay proportional to $t^{-1.26\pm0.05}$. This plot also clearly illustrates that self-similar decay is achieved after $\tau = 40$, as assumed in the earlier computations of θ.

The molecular mixing fraction Θ and the mixing parameter Ξ are defined as

$$\Theta = \frac{\int \langle f_1 f_2 \rangle \, \mathrm{d}x}{\int \langle f_1 \rangle \langle f_2 \rangle \, \mathrm{d}x}, \quad \Xi = \frac{\int \langle \min(f_1, f_2) \rangle \, \mathrm{d}x}{\int \min(\langle f_1 \rangle, \langle f_2 \rangle) \, \mathrm{d}x}. \tag{4.4}$$

where $\langle f_{1,2} \rangle$ indicates the y–z plane-averaged volume fraction of species 1, 2, where species 1 is the heavy gas. Here Θ gives a guide to the total reaction rate for a slow reaction and Ξ is an equivalent measure for a fast reaction rate where one reactant is fully depleted. Figure 11 shows these quantities plotted for all grid resolutions. As grid size increases both Θ and Ξ decrease; however, the molecular mixing fraction Θ and the mixing parameter Ξ both approach a constant state. The asymptotic values of $\Theta = 0.84 \pm 0.02$ and $\Xi = 0.84 \pm 0.01$ are similar to previous turbulent mixing

Domain length	N_x	$N_y = N_z$
8π	256	64
4π	256	128
4π	512	256
2.8π	720	512

TABLE 2. Grid sizes employed for the $At^+ = 0.9$ case.

simulations of the related Rayleigh–Taylor instability by Youngs (2003) and Cook & Zhou (2002).

5. Narrowband initial conditions at Atwood 0.9

The initial conditions employed in the previous section were modified to examine the influence of Atwood number. The initial conditions for the $At^+ = 0.9$ case were chosen to give the same initial linear impulse as those for the lower Atwood case, i.e. for the low Atwood case the initial velocity can be written as

$$\frac{\mathrm{d}a}{\mathrm{d}t} = k\Delta u a_0 At^+ = 14ka_0. \tag{5.1}$$

It is useful to maintain ka_0 the same as the lower Atwood case to avoid issues with nonlinear initial amplitudes of the modes. As the behaviour of the RM instability is considered to be relatively insensitive to shock Mach number, it was decided to modify Δu to compensate for the increase in At^+. Given that $At^+ = 0.9$, the required $\Delta u = 15.555$. Choosing the heavy gas to have a dimensionless density of 20 and the light gas of density 1 gives a required shock Mach number of 1.91 in the heavy gas to maintain the same initial growth rate. A consequence of the high density of the second material is that there are compressibility effects at very early times due to the low sound speed in the dense fluid, where the initial growth is supersonic (Mach ≈ 1.2). An additional simulation was run in CNS3D at the highest resolution, where the initial pressure has been increased by a factor of 10 to ensure that the turbulent fluctuations remain below Mach 0.4. The shock Mach number was decreased to 1.245 to maintain the same Δu. The TURMOIL3D simulation with velocity perturbation was initialized with the higher pressure. There is some uncertainty in the quantitative comparison of the two initial conditions as there is a scaling factor introduced related to the compression of the two fluids by the shock but this should not affect the self-similar properties such as θ or the scaled volume fraction profile.

The effect of the resolution on the initial perturbation was investigated by first fixing the initial perturbation at $\lambda_{min} = 16\Delta x$ and running this on a 64 cross-section grid, then increasing the resolution up to a 256 cross-section grid with the same initial wavelength, i.e. $\lambda_{min} = 64\Delta x$. Comparing the integral width predicted from the 256 cross-section with that predicted from the 64 cross-section shows that it does not vary significantly especially considering the improved resolution of the initial modes in a highly nonlinear system. From this it was concluded that the simulations at high Atwood were reasonably converged with $\lambda_{min} = 16\Delta x$.

As there is a greater momentum on the spike side than in the previous simulations, the domain size must be increased at lower grid resolutions to allow a greater simulation time. Thus, the domain sizes chosen were longer than those in the lower Atwood case. The cross-section was fixed at 2π and the individual cells were cubic in all cases. The resolutions employed are detailed in table 2. As the grid resolution

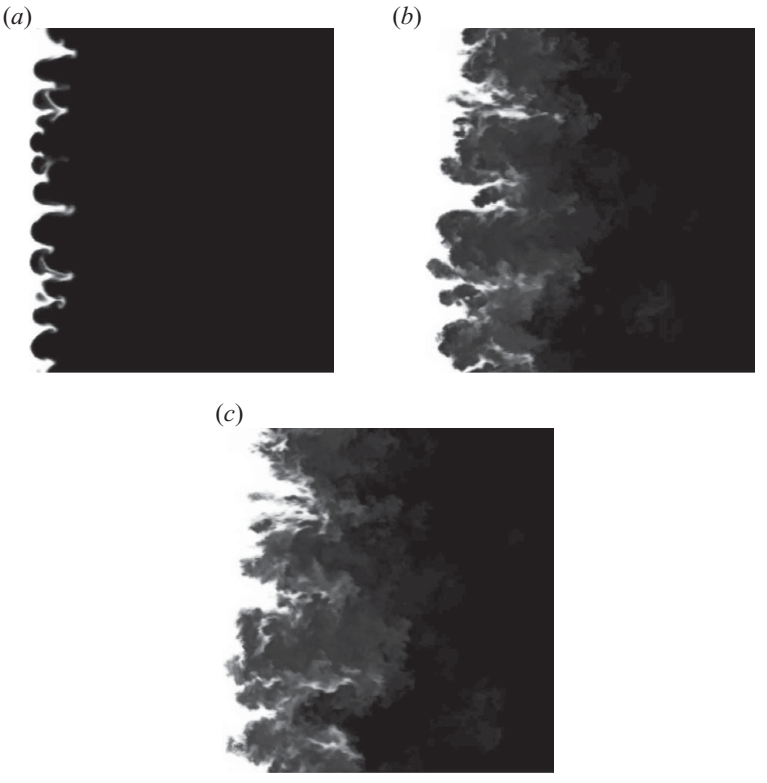

FIGURE 12. Two-dimensional visualizations of the evolution of the volume fraction for the $At^+ = 0.9$ narrowband perturbations at $\tau = 7.4,\ 100$ and 227 using CNS3D at $512 \times 256 \times 256$ resolution.

increases, the initial growth rate is lower; hence, the domain length can be reduced to allow more efficient computation.

Visualizations of the flow field are shown in figures 12–14 for the 256 cross-section. The initial times show a significantly narrower spike when compared to the lower Atwood case, as clearly illustrated in figure 12; however, the same mushroom-shaped features and ring vortices are observed. At later times, the distribution of vortices highlighted by isosurfaces of Q in figure 14 shows a homogeneous layer with a wide range of scales illustrated by the volume fraction isosurfaces in figure 13.

Figure 15 shows the convergence of the integral width as the grid resolution increases. Note that the integral width W for the CNS3D simulation with a higher background pressure (lower Mach) has been rescaled to take into account the different post-shock interface amplitudes (approximately 16 % larger than the higher Mach case). As with the lower Atwood case, the integral width converges at approximately 128 cross-section. Using the nonlinear regression technique described in the previous section on the CNS3D data applied to all data points gives $A = 0.22$, $t_0 = 2.4$ and $\theta = 0.264$. Applying regression to all points after $\tau = 400$ gives the same value of $\theta = 0.3$, $A = 0.17 \pm 0.01$ and $t_0 = -60 \pm 20$.

Calculating these parameters for the results generated with CNS3D using the first and second derivatives of W as described in (4.2) gives the same mean values as the above; however, it appears that the values of both t_0 and A are progressively decreasing with time, while θ levels off at 0.3. These estimations are close to those

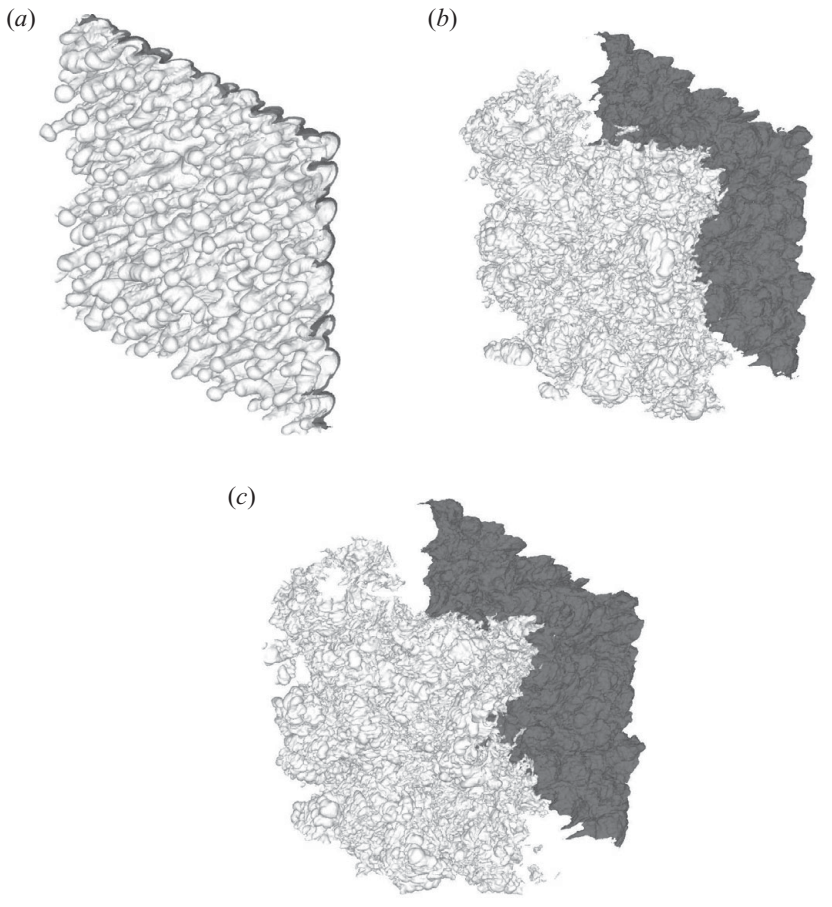

FIGURE 13. Isosurfaces of volume fractions 0.999 and 0.001 for the $At^+ = 0.9$ narrowband perturbations at $\tau = 7.4$, 100 and 227 using CNS3D at $512 \times 256 \times 256$ resolution.

computed for the previous $At^+ = 0.48$ case and do not exhibit the large exponents observed in the experiments by Dimonte & Schneider (2000) at similar Atwood numbers (with immiscible fluids). As expected, there are some minor differences between TURMOIL3D and CNS3D for this case, which can be attributed to the difference in the initialization of the problem (velocity perturbation versus shock perturbation), as discussed in Appendix B. For TURMOIL3D, the value of θ is still evolving at the latest time, changing from $\theta = 0.273$ for data fits including early times to $\theta = 0.254$ for a data fit from $\tau = 300$ onwards.

The plane-averaged volume fractions are shown in figure 16 for the 512 cross-section resolution. At early times, the bubble side (negative x/W) is very close to being self-similar. To highlight this process, the quantity $\langle f_1 \rangle (1 - \langle f_1 \rangle)$ has also been plotted in figure 16. It illustrates that at larger plane-averaged volume fractions ($\langle f_1 \rangle (1 - \langle f_1 \rangle) > 10^{-3}$), the mixing layer is self-similar on the bubble side from early times.

However, there is a significant variation on the spike side indicating that the self-similar behaviour of the spike only appears at a very late time. This is clear by comparing figure 16 with figure 8, where the lower Atwood case shows a much better convergence at the same dimensionless time. At early time, the dimensionless width

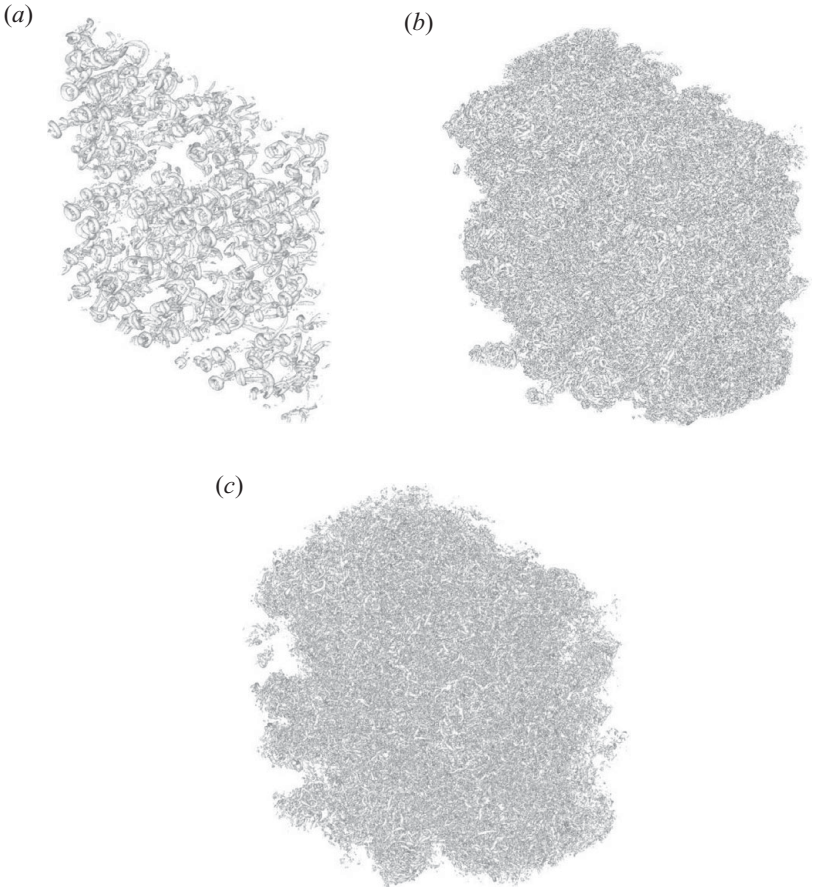

FIGURE 14. Visualization of vortex cores using $Q = 500$ at early time, $Q = 5$ for the two later times for the $At^+ = 0.9$ narrowband perturbations at $\tau = 7.4$, 100 and 227 using CNS3D at $512 \times 256 \times 256$ resolution.

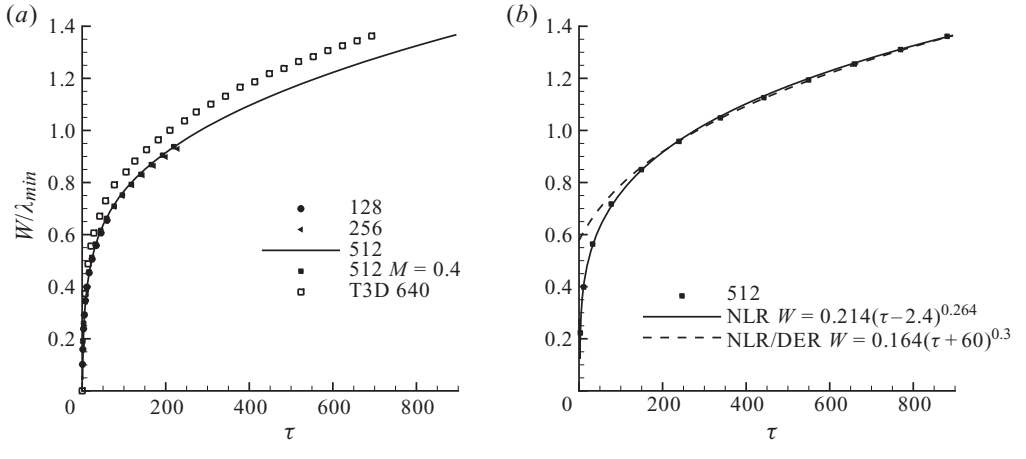

FIGURE 15. Variation of integral width with respect to grid resolution for the $At^+ = 0.9$ narrowband initialization (a) and with analytical data fits (b).

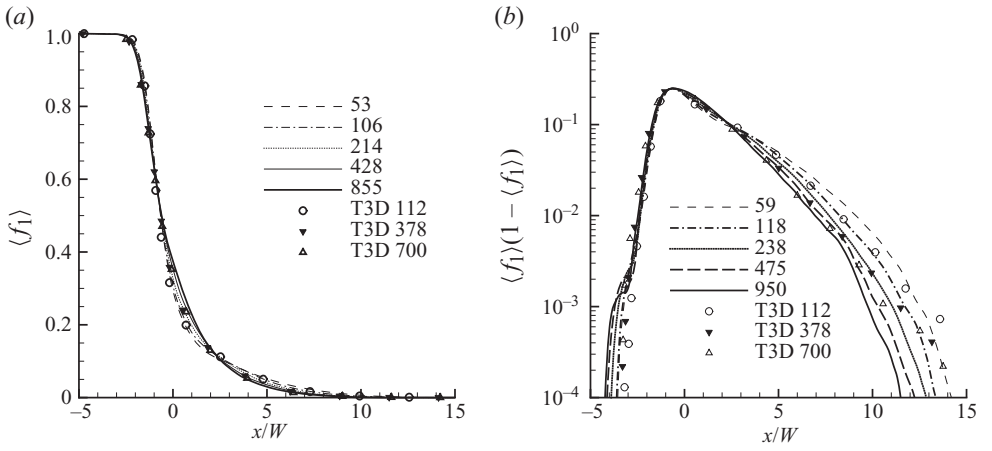

FIGURE 16. Profiles of (*a*) plane-averaged volume fractions $\langle f_1 \rangle$ of species one plotted against normalized distance and (*b*) $\langle f_1 \rangle (1 - \langle f_1 \rangle)$ plotted against normalized distance for the 512 cross-section simulation at different dimensionless times for the $At^+ = 0.9$ narrowband case.

of the spike side is larger, due to the momentum of relatively coherent vortex rings ejected from the mixing layer in the initial interaction process. These are generated in regions where interaction with nearby modes in wavenumber space is relatively low, permitting the appearance of undistorted rings. At later times, these become unstable, breaking down and eventually becoming part of the mixing layer leading to a narrower dimensionless plane-averaged volume fraction distribution as can be seen at $\tau = 950$.

Although the high Atwood simulation was designed to have the same initial linear velocity impulse as the lower Atwood case, it has a higher momentum; hence, the parcels of the dense fluid advected by the vortex rings travels farther. This effect is stronger in the TURMOIL3D simulation, leading to a higher volume fraction at distances farther from the mixing layer. As the vortex rings structures typically span 20 computational cells, they do not evolve independently of the influence of numerical viscosity; hence, there is an element of scheme dependence. The finite-difference method in the semi-Lagrangian code preserves these coherent small-scale structures, whereas the Godunov method predicts that these structures will become unstable and break down.

These vortex rings provide a source of intermittency, contributing their own characteristic time scale to the overall evolution of the mixing-layer width. The co-existence of two different scaling laws within the same mixing layer is potentially the cause of the high values of θ observed in the linear electric motor experiments by Dimonte & Schneider (2000) at high Atwood number. Simulations indicate that only a small amount of material is carried with each vortex ring and that at late time they are reabsorbed into the mixing layer, which then develops in a fully self-similar manner.

Figure 17 shows the average of 10 two-dimensional fluctuating kinetic energy spectra taken in the y–z plane about the peak of fluctuating kinetic energy in the mixing layer for the v and w velocities, and the u velocity. The spectrum of the v and w velocities shows both a $k^{-5/3}$ and a $k^{-3/2}$ range. The Kolmogorov inertial range is present for $80 \leqslant k \leqslant 200$ at the latest time, and the $k^{-3/2}$ range is present for $18 \leqslant k \leqslant 80$. At early times ($\tau = 237$, the third line down in figure 17), the $k^{-3/2}$ range is slightly longer, extending to $k = 150$, but is 'eaten away' by the sub-inertial range at

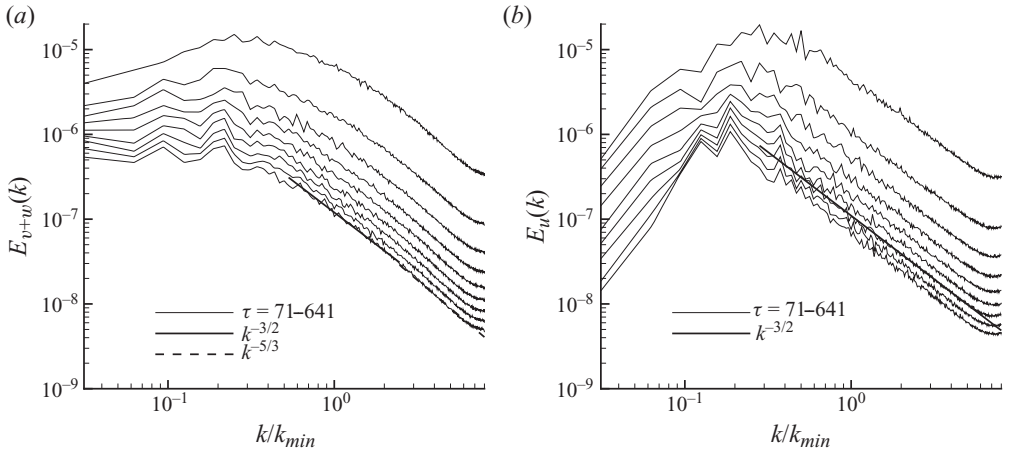

FIGURE 17. Fluctuating radial kinetic energy spectra for the 512 cross-section $At^+ = 0.9$ narrowband simulation at $At^+ = 0.9$ from $\tau = 79$ to 950 in increments of $\delta\tau = 79$ for (a) the $v + w$ components and (b) the u component.

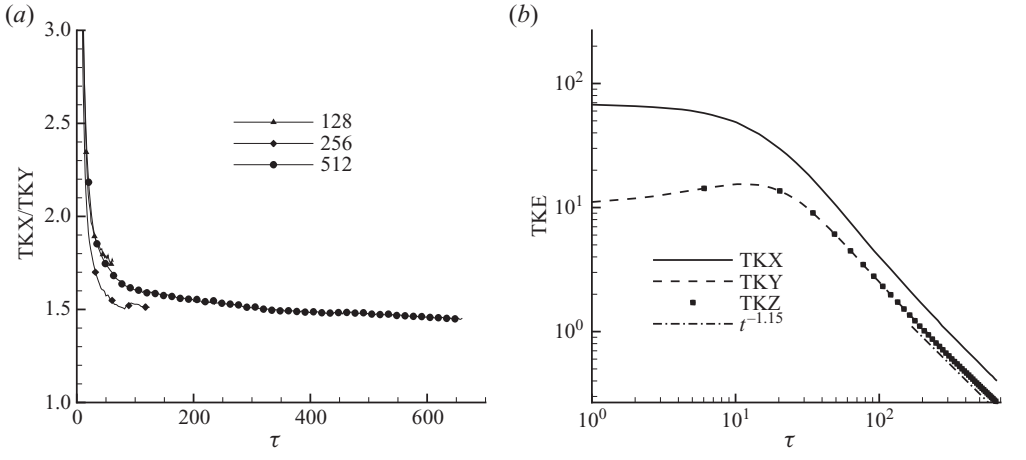

FIGURE 18. Plots of (a) ratio of fluctuating kinetic energies and (b) plot of x-, y- and z-directions total kinetic energy for the 512 cross-section narrowband simulation at $At^+ = 0.9$.

later times. There is a clear difference in the behaviour of the velocities in the shock direction as compared to the transverse velocities. As with the lower Atwood case, the spectrum of the u velocity in the homogeneous direction shows a $k^{-3/2}$ behaviour, and the low wavenumber portion of the spectrum drops off more sharply than that of the transverse spectrum.

The decay of fluctuating kinetic energy and the ratio of the parallel to transverse components are plotted in figure 18. The turbulent kinetic energy is decaying at a rate proportional to $t^{-1.15}$, with an expected margin of ± 0.1 as the decay law is not as consistent as in the lower Atwood number case. This translates to $\theta = 0.28 \pm 0.03$, which is within the range predicted by the various integral width line fitting methods. The ratio of kinetic energies appears to be levelling off more slowly than that in the lower Atwood case. This is expected as the rate of growth of Kelvin–Helmholtz

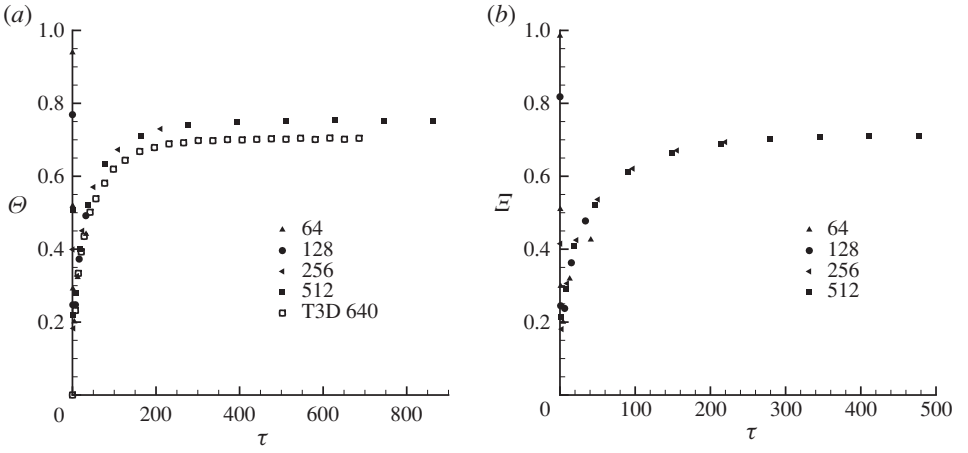

FIGURE 19. Molecular mixing parameters (*a*) Θ and (*b*) Ξ for the $At^{+}=0.9$ narrowband perturbation at different grid resolutions.

unstable modes is proportional to $\sqrt{\rho_1\rho_2}/(\rho_1+\rho_2)$, which is lower when the two fluids have different densities, leading to a slower transfer of fluctuating kinetic energy.

The molecular mixing fraction Θ and the mixing parameter Ξ are plotted in figure 19. At this Atwood number, the asymptotic values of the mixing parameters are reduced: $\Theta=0.73\pm0.02$ and $\Xi=0.70\pm0.02$. This reduction in mixing efficiency is in agreement with the observation that the growth rate of Kelvin–Helmholtz unstable modes is reduced as compared with the lower Atwood case. Additionally, both Θ and Ξ take longer to asymptote to a statistically steady state.

TURMOIL3D has a lower Θ indicating that there is less mixing – consistent with the observation that the spikes do not break down as rapidly in the semi-Lagrangian methodology. Previous experience with the two numerical methods applied to homogeneous decaying turbulence has shown that the semi-Lagrangian method is moderately over-dissipative at high wavenumbers, whereas the modified Godunov method in CNS3D is slightly under-dissipative. This indicates that small-scale features in CNS3D are more likely to break down, whereas in TURMOIL3D they remain coherent. For this reason, it is probable that the actual value of Θ lies within the limits laid down by the two codes, i.e. $0.71\leqslant\Theta\leqslant0.75$. Note that the value of Θ is a measurement that is especially sensitive to small variations in the profile of $\langle f_1 f_2\rangle$.

6. Broadband initial conditions at Atwood 0.5

6.1. *Flow phenomenology*

Figure 20 shows six density slices at different time instants in the evolution of the mixing layer at the highest resolution employed (over 3×10^9 points). The first time instants show the initial growth of the mixing layer that is dominated by the highest wavenumbers that rapidly saturate. As time continues, progressively longer and longer wavelengths grow linearly, saturate and become turbulent. Note that at the latest time simulated, there is no significant perturbation of the interface at wavelengths close to the longest wavelength excited. This is important as it confirms that the simulation considers a reasonable length of time during which the shortest wavelengths have saturated, but the longest wavelengths have not yet grown to nonlinear amplitude.

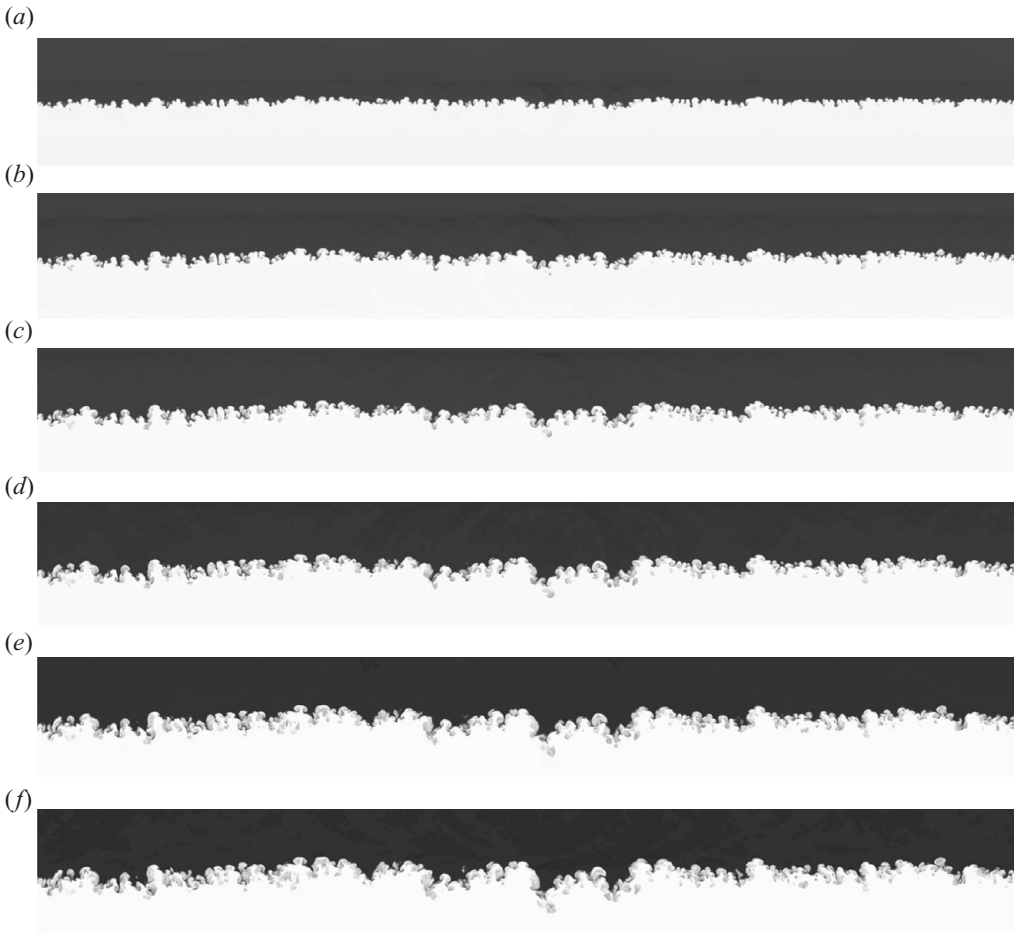

FIGURE 20. Two-dimensional slices showing the evolution of density for the $At^{+}=0.5$ broadband perturbations at $\tau=8$, 16, 24, 32, 40 and 48 using CNS3D at $720\times2048\times2048$ resolution.

Figure 21 shows a three-dimensional rendering of isosurfaces of volume fraction for the 2048 cross-section. Figure 22 shows the 'Q' criterion highlighting the vortex cores within the mixing layer in a 256 subsection of the 512 simulation. Compared to the narrowband simulations, a range of perturbation length scales grow simultaneously, as is shown clearly in figure 20. As successively larger modes dominate the growth, they can be seen emerging as bubbles in the three-dimensional plots of volume fraction isosurfaces.

Examining the vortices highlighted in figure 22, note that at $\tau=56$ the flow field consists of many coherent vortex structures. At this point, the simulation is just about to transition from being a mixing layer dominated by the growth of successively large modes to a fully developed two-dimensional turbulent mixing layer. Hence, at the final time instant ($\tau=294$), the distribution of vorticity in the mixing layer begins to resemble the earlier narrowband simulations. A key difference is that the vorticity is not as evenly distributed when compared to the narrowband case, which is to be expected as the structures in the narrowband case have been generated by high wavenumber perturbations, naturally leading to a smoother, more regular

λ_{max}	N_x	$N_y = N_z$	θ
$L/2$	90	64	—
$L/2$	180	128	0.42
$L/2$	360	256	0.48
$L/2$	720	512	0.54
$L/2^T$	700	1024	0.58
$L/2^*$	360	1024	0.59
$L/2^*$	720	2048	0.62

TABLE 3. Values of θ computed from derivatives of W as a function of grid resolution. The asterisk (*) indicates reduced domain length, and the superscript (T) indicates simulation run with TURMOIL3D.

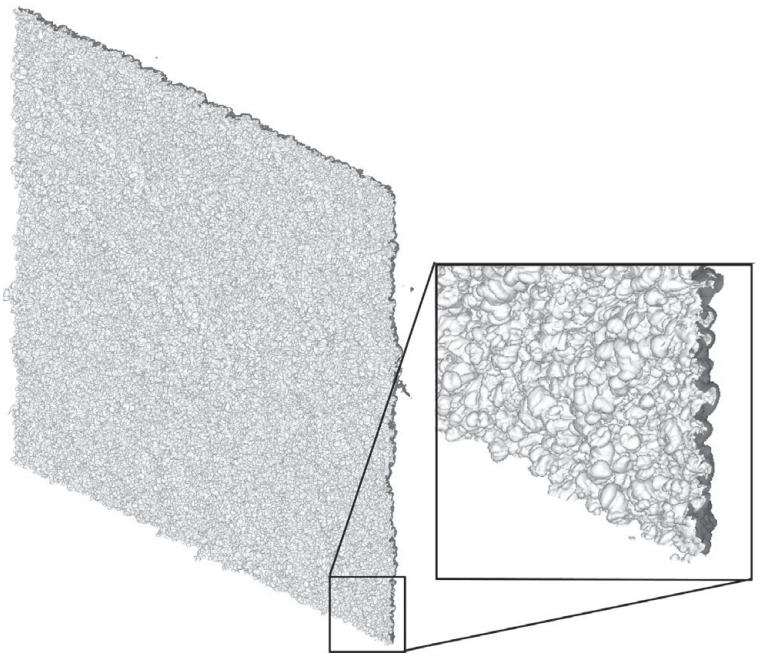

FIGURE 21. Isosurfaces of volume fractions 0.99 and 0.01 for the $At^+ = 0.5$ broadband perturbation at $\tau = 48$ using CNS3D at $720 \times 2048 \times 2048$ resolution.

distribution. Additionally, to satisfy energy arguments discussed in § 2.2.2, there must be regions of high and low turbulent kinetic energy so that the overall growth rate of the mixing layer can be higher than that theoretically predicted and numerically simulated for a homogeneous layer.

6.2. *Flow physics*

The variation of the integral width as a function of time and grid resolution is plotted in figure 23 for the three highest grid resolutions. In addition, table 3 documents the value of θ computed for each grid resolution. Clearly, there is a strong variation in the values of θ dependent on the ratio of the longest to the shortest wavelengths – varying from $\theta = 0.42$ at 128 cross-section to $\theta = 0.62$ at 2048 cross-section.

The values of θ are converging gradually towards $\theta \approx 2/3$ as predicted by Youngs (2004) through consideration of the growth envelope of a series of successively

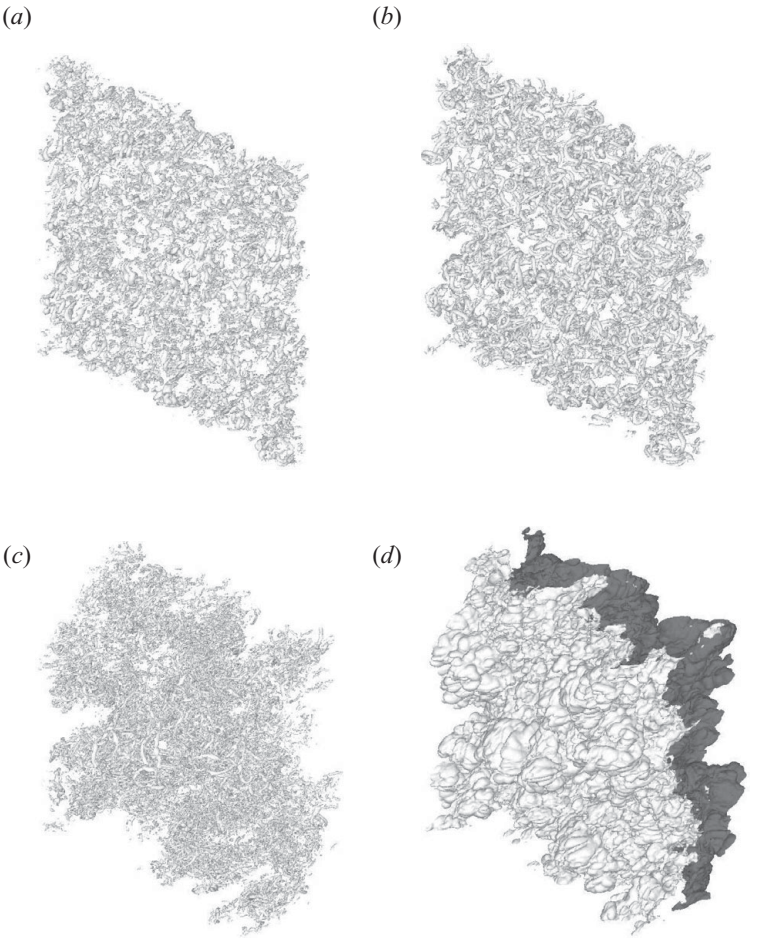

FIGURE 22. Visualizations of vortex cores using the Q criterion in a 256×256 section of the CNS3D simulation at $720 \times 512 \times 512$ simulation showing the evolution of the volume fraction for the $At^{+} = 0.5$ broadband perturbation at $\tau = 12$, 56 and 294. The final image (d) shows the volume fraction isosurfaces at the final time in the reduced section.

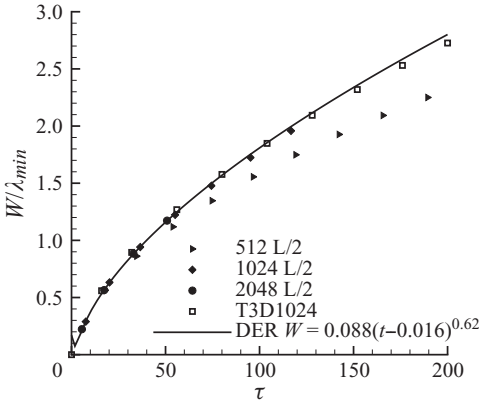

FIGURE 23. Variation of integral width with respect to grid resolution and λ_{max} for the $At^{+} = 0.5$ broadband perturbation.

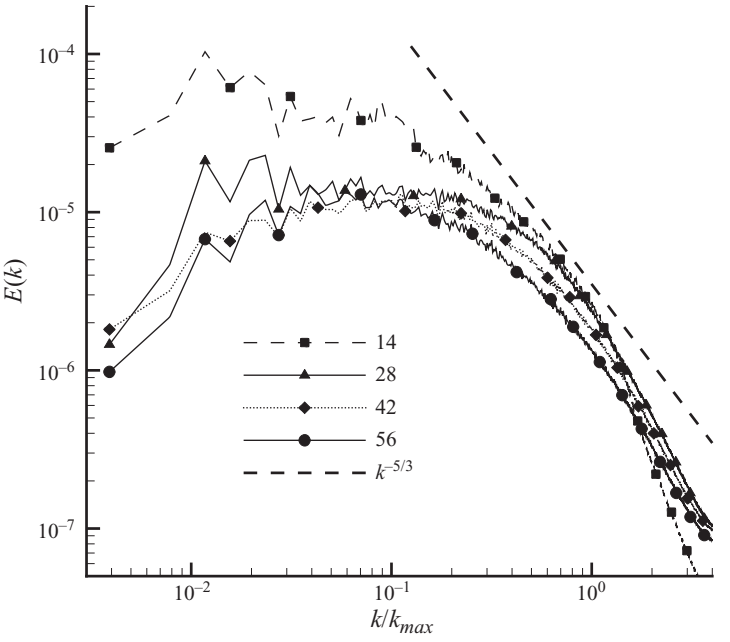

FIGURE 24. Fluctuating kinetic energy spectra for the 2048 cross-section $At^{+} = 0.5$ broadband simulation at different dimensionless times.

emerging modes. As this growth rate is larger than the growth rate of a slab of homogeneous turbulence (the narrowband case), the growth due to the linear momentum of successively larger modes dominates. This strongly supports the representation of mode interference proposed by Youngs.

The fact that the value of θ has not converged completely at such high grid resolution demonstrates the extreme sensitivity of the problem to the initial conditions. Given that the largest wavelength is 128 times the size of the smallest wavelength in the 2048 cross-section simulation, and yet self-similar growth is achieved only for a very short period of time, implies that experiments/simulations that do not have an appropriately broad spectrum of initial perturbations may not achieve a long duration of self-similar growth. Given a short spectral range of initial perturbations, the growth rate will not approach the expected 'asymptotic' value of θ, but will lie somewhere in between that expected from a narrowband perturbation and the theoretical value for a 'full' spectrum. This is equally applicable to the final design of a fusion capsule. The fact that the time of self-similar growth is so short is linked to the observation that linear growth of a single mode following Richtmyer's formula is accurate to approximately $ka = 0.15$ (compared to nonlinear theory of Zhang & Sohn 1997). Hence, even at such small amplitudes, the growth of the mode begins to slow and is overtaken by longer wavelength modes.

The principal aim of the choice of initial conditions was to maximize the period of time during which the mixing layer is self-similar in behaviour, i.e. when the mode that is currently dominating the growth of the mixing layer lies between small scales that are fully saturated and large scales that have not yet grown significantly. To verify that this was the case, the two-dimensional turbulent kinetic energy spectra have been computed in the y–z plane at the centre of the mixing layer (in the plane normal to the direction of the shock propagation). The results are shown in figure 24 for the 2048 cross-section at several time instants.

At $\tau = 14$, the large scales have quite a large amount of energy compared with later times when the spectra are flat at low wavenumbers. At the earliest time, the shock is significantly non-planar due to the interaction with the perturbed material interface, generating an additional fluctuating velocity. At later times, the spectra are constant for $1 \times 10^{-2} \leqslant k/k_{max} \leqslant 0.4$, equivalent to $3 \leqslant k \leqslant 102$. That this should be the case can be shown analytically. The initial velocity for each mode in Fourier space is given by Richtmyer's theory $\dot{a} = k\Delta u a_F At$, where the amplitude of each mode in Fourier space $a_F^2 \approx P(k)$. As the initial perturbation spectrum for the 2048 cross-section was of the form $P(k) \propto 1/k^2$ between $2 \leqslant k \leqslant 256$, then it would be expected that the fluctuating kinetic energy spectra would be constant between these wavenumbers once the shock has passed through the mixing layer, i.e. $\dot{a} = k\Delta u At/k =$ constant. The range in figure 24 is slightly smaller than this as the high wavenumber end breaks down rapidly, passing its energy to even smaller vortices, and the statistics of the low wavenumber end are not sufficient to generate a smooth constant line.

After the passage of the shock wave, the high wavenumber end of the spectrum fills with energy from the excited modes, a process that is most noticeable between the first two time instants plotted. The initially flat plateau is 'eaten away' at the high wavenumber end by the transfer of energy to the highest wavenumbers and subsequent dissipation. A $k^{-5/3}$ sub-inertial range has begun to develop in the last time instant, spreading from the high wavenumber end of the plateau to $k \approx 512$, becoming longer as the mixing layer develops.

In the 512 cross-section resolution simulation which ran to late times, a Kolmogorov $k^{-5/3}$ sub-inertial range can be seen at high wavenumbers. The analysis of Zhou (2001) can be modified to take into account the effects of the initial perturbation spectrum. To do this, the characteristic external time scale associated with RM mixing is written using a characteristic velocity dependent on the initial conditions. Following Youngs (2004), for an initial power spectrum of the form $P(k) \propto Ck^m$, the velocity of each mode can be written as $\dot{a} = At\Delta u k^{(m+2)/2}$. Defining the characteristic time $\tau_{RM} = 1/k\dot{a}$, the kinetic energy spectra can be written as

$$E(k, z) = C_{RM}\epsilon^{1/2}\tau_{RM}^{-1/2}k^{-2} = C_{RM}\epsilon^{1/2}\Delta u At k^{(m-6)/4}; \tag{6.1}$$

hence for $m = 0$ this reduces to $k^{-3/2}$ as proposed by Zhou (2001); however, it now includes the influence of initial conditions. For a k^{-2} perturbation power spectrum, this predicts an inertial range of the form $E(k) \propto k^{-2}$, assuming that $\tau_{RM} < \tau_{HDT}$, where τ_{HDT} is the characteristic eddy turnover time in a homogeneous decaying turbulence. If this is not satisfied then the spectra should revert to $k^{-5/3}$. This is not seen at the latest times for the 2048 cross-section, or past the saturation of the longest mode in the 512 cross-section, where a $k^{-5/3}$ range is observed. A potential explanation is that when the line of the predicted kinetic energy spectrum is lower than that which would be generated by turbulent breakdown of the large scales, a $k^{-5/3}$ spectrum is observed. If this is the case, then the inertial range spectrum of an RM instability would only be sensitive to initial conditions for $m \geqslant -2/3$ – as it is in the narrowband case. An alternative explanation would simply be that the grid resolution is not high enough to achieve a 'universal' inertial range at high wavenumbers (as we have a very wide range of 'large eddies'), or that one only appears at later times.

Figure 25 shows the plane-averaged volume fraction profiles at different dimensionless times for the highest grid resolution. The x-direction has been normalized by the integral width to check for self-similarity in the profiles. The spike (heavy fluid penetrating into light fluid) side of the mixing layer rapidly achieves a self-similar behaviour (after $\tau = 2$); however, the bubble side does not become self-similar until after $\tau = 14$ – in contrast to the behaviour observed in the narrowband simulations. Once the

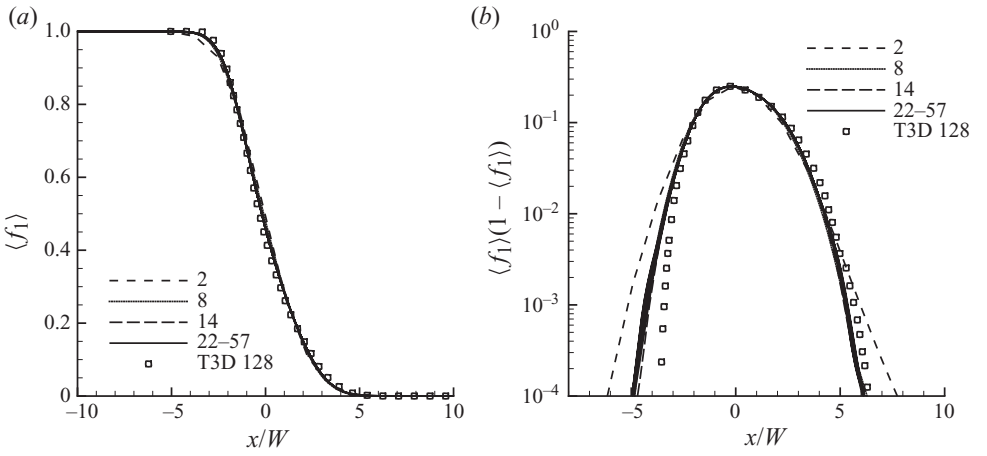

FIGURE 25. Profiles of (*a*) plane-averaged volume fractions $\langle f_1 \rangle$ of species one plotted against normalized distance and (*b*) $\langle f_1 \rangle (1 - \langle f_1 \rangle)$ plotted against normalized distance for the 2048 cross-section CNS3D simulation and the 1024 TURMOIL3D at different dimensionless times. Note that the solid line is actually a plot of 10 separate time instants equally spaced between dimensionless times of 22 and 57.

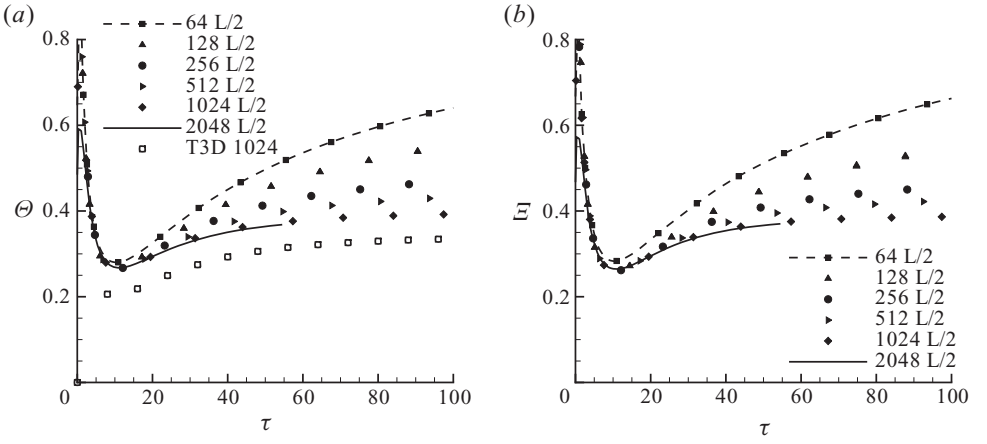

FIGURE 26. Molecular mixing parameters (*a*) Θ and (*b*) Ξ for the $At^+ = 0.5$ broadband perturbation at different grid resolutions.

bubble has settled into the self-similar behaviour, the plane-averaged volume fraction does not change at all for $22 \leqslant \tau \leqslant 57$, as shown in figure 25 where the profiles for 10 time instants equally spaced between 22 and 57 lie on top of each other. Additionally, figure 25 shows a plot of $\langle f_1 \rangle (1 - \langle f_1 \rangle)$ to highlight the convergence of the flow field at the extremes of the mixing layer. Unlike the high Atwood number case, the extremes of the mixing layer converge extremely rapidly to self-similar behaviour for $\tau \geqslant 27$. This further demonstrates that at this grid resolution a self-similar growth exists within the duration of the simulation. Note that the TURMOIL3D results are presented after the saturation of the longest wavelengths; hence, it is expected that the flow physics will be in transition between the broadband case and a slab of decaying turbulence.

Figure 26 illustrates the mixing parameters Θ and Ξ for the broadband perturbation at all of the grid resolutions. Unlike the narrowband case, there is much slower grid

convergence of the results – as observed with the convergence of the integral mix width; however, at the highest two grid levels there is little variation, implying that the results are almost converged at $\Theta \approx 0.37$ and $\Xi \approx 0.38$. TURMOIL3D results are lower, predicting $\Theta \approx 0.33$. This is significantly lower than the narrowband case, indicating that there is less mixing of the two fluids despite the more rapid growth of the mixing layer. It is conjectured that the decreased mixing rate is caused as the fluids do not interact turbulently at the driving scale (which is essentially a superposition of modes), but mix at a scale that is below the driving scale, leading to a lower molecular mixing efficiency. This is linked to the observation that the mixing layer cannot be uniformly mixed and have a growth rate approaching $\theta = 2/3$ from conservation arguments.

7. Conclusions

This paper has investigated the influence of initial conditions on the rate of growth of a Richtmyer–Meshkov-induced turbulent mixing layer through a series of carefully designed numerical experiments. Results were presented for a succession of increasingly fine grid levels from 4×10^5 to 3×10^9 grid points, with two different numerical methods.

The key conclusion is that the growth of the resultant mixing layer is strongly dependent on initial conditions, following the theory developed by Youngs (2004). This highlights the importance of separating the two cases of a homogeneous turbulent mixing layer, and a turbulent mixing layer that is driven by non-turbulent fluctuations caused by broadband perturbations.

The narrowband simulation at $At = 0.5$ showed excellent agreement with LEM experiments, giving $\theta \approx 0.26$, which is also in good agreement with accepted theory for growth of a turbulent slab by mode coupling. Increasing the Atwood number to 0.9 gave only a minor increase in θ for both numerical methods, due to a slower rate of breakdown of the initial RM-induced growth by Kelvin–Helmholtz shear instabilities. At the higher Atwood number, individual vortex rings containing a small amount of heavy material propagate farther into the light material. This adds a second characteristic time scale to the problem, and it is conjectured that these vortices increase the values of θ on the spike side observed in experiments. However, simulations indicate that at late time they will be absorbed by the mixing layer. Both cases exhibit a $k^{-3/2}$ kinetic energy spectrum in agreement with the analysis of Zhou (2001).

Simulations of the broadband initial conditions resulted in increased growth of the mixing layer up to $\theta = 0.62$ at the highest grid level. It is asymptoting towards the theoretical value of $\theta = 2/3$ and shows that the enhanced growth rates predicted by laser experiments (Dimonte & Schneider 1997) can be due to the presence of a broadband range of perturbations. However, a key observation is that this theoretical value is only achieved when the simulation has a sufficient range of initial wavenumbers in the perturbation. Theoretical and numerical analyses demonstrate that there is a surprisingly short period of time between the saturation of the highest wavenumbers initialized and the saturation of the lowest wavenumbers. This requires a very high numerical resolution – indeed the current simulations demonstrate that the self-similar regime is not properly reached until grids with cross-sections of 2048×2048. It implies that it is not possible to conduct accurate LES of this flow at lower grid resolutions without resorting to artificial forcing terms that significantly enhance the growth of the mixing layer. At the highest grid resolution, for the

broadband case the kinetic energy spectra follow the expected $E(k) \approx$ const. over the range of initial perturbations. As a consequence of the inhomogeneity of the resultant mixing layer, the mixing parameters are significantly lower than those for the narrowband case.

Future work will focus on the understanding of the capability of numerical methods to model the breakdown of a single vortex ring, as the rate of breakdown of these vortices influences greatly the (albeit small) volume fraction at large distances from the centre of the mixing layer. Of key interest is the accurate determination of the mixing fractions for the high Atwood case, which potentially requires the use of a fully incompressible LES code. Additionally, it would be interesting to examine a different power spectrum in the broadband case, where $P \propto Ck^{-3}$, which should give a theoretic growth rate of $\theta = 1$ – this would further confirm the theory of Inogamov (2006) and Youngs (2004). Finally, the results from the LES performed here are being used to extend and improve current RANS methodologies for shock-induced turbulent mixing.

The authors would like to acknowledge the financial support from EPSRC, MoD and AWE through the EPSRC (EP/C515153)-JGS(no. 971) project, as well as EPSRC in relation to computational resources (project EP/D053994/1). The computations were run on Cranfield's Astral supercomputer and AWE's Redwood facility.

Appendix A. Initialization of perturbed interface

A.1. *Analytical Fourier transform*

This appendix details the analytical Fourier transform employed to transform the given surface power spectrum into a perturbation in physical space. The particular case considered in this paper involves a power spectrum of the form

$$P(k) = \begin{cases} Ck^m, & k_{min} < k < k_{max}, \\ 0, & \text{otherwise}, \end{cases} \tag{A 1}$$

where $k = \sqrt{k_y^2 + k_z^2}$ is the wave vector of the perturbation. First, the power spectrum is rewritten as a two-dimensional power spectrum in wave space as

$$\sigma^2 = \int_0^\infty P(k)\mathrm{d}k = \int_{-\infty}^{\infty}\int_{-\infty}^{\infty} \frac{1}{2\pi}\frac{P(k)}{k}\,\mathrm{d}k_y\,\mathrm{d}k_z. \tag{A 2}$$

The specified power spectrum gives an equivalent amplitude $a(\boldsymbol{k})$ in wave space:

$$a(\boldsymbol{k}) \propto \sqrt{\frac{P(k)}{k}}. \tag{A 3}$$

To initialize modes within a certain band, the inverse Fourier transform of this relation can be taken, noting that the amplitude is a real function, as

$$A(y, z) = \sum_{m,n=-N}^{N} \mathrm{Re}\left\{c_{m,n} \exp\left[\mathrm{i}k_0\,(my + nz)\right]\right\}, \tag{A 4}$$

where $k_{max} = 2N\pi/L$, the cross-section is $L \times L$ and $c_{m,n}$ are the amplitudes of the mode with wavenumbers m in the y-direction and n in the z-direction. To satisfy the given power spectrum, (A 4) can be simplified considerably by expanding, using the

Euler formula, and considering only the real part,

$$A(y,z) = \sum_{m,n=0}^{N} a_{m,n}\cos(k_0 m y)\cos(k_0 n z) + b_{m,n}\cos(k_0 m y)\sin(k_0 n z) + c_{m,n}\sin(k_0 m y)\cos(k_0 n z) + d_{m,n}\sin(k_0 m y)\sin(k_0 n z). \quad \text{(A 5)}$$

To initialize a random field, $a_{m,n}$, $b_{m,n}$.... must be chosen from a distribution randomly so that the standard deviation is proportional to the Fourier coefficients in (A 3). The random variables are selected from a Gaussian distribution to give the desired mean amplitude at a given wavenumber $k_{m,n}$, in this case

$$\frac{1}{4}\left(\bar{a}_{m,n}^2 + \bar{b}_{m,n}^2 + \bar{c}_{m,n}^2 + \bar{d}_{m,n}^2\right) = \frac{1}{2\pi}\frac{P(k_{m,n})}{k_{m,n}}\Delta k_y \Delta k_z, \quad \text{(A 6)}$$

where $k_{m,n} = \sqrt{k_{ym}^2 + k_{zn}^2}$, the wavenumber in the y-direction is $k_{ym} = 2\pi m/L$, the wavenumber in the z-direction is $k_{zn} = 2\pi n/L$ and L is the width of the domain that in this case is assumed to have a square cross-section.

A.2. *Ensuring linearity*

A key issue in the initialization is to ensure that the initial condition itself is linear – in which the amplitude of the mode of a wavenumber k is significantly less than the wavelength. Noting that the power spectrum of the initial condition satisfies (A 2), the physical amplitude of a given wavenumber $a_k = 2\sigma_k$, where σ_k is the root-mean-square amplitude in a band around wavenumber k, can be approximated as

$$a_k^2 \approx 4\int_{k/2}^{k} P(k')\,\mathrm{d}k' \approx 4kP(k). \quad \text{(A 7)}$$

If it is assumed that the modes are linear if $ka_k = 1/2$, hence, from (A 7), $P(k)$ must have the form $P_{lin}(k) = a_k^2/4k = 1/16k^3$. This defines a curve P_{lin} in wavenumber space above which the amplitude of the modes is approximately nonlinear, below which the amplitude is linear. As the initializations chosen for this paper have an initial spectrum $P(k) = C$ and $P(k) = Ck^{-2}$, the coefficient (c) must be chosen carefully to ensure that $P(k)$ does not cross the curve defined by P_{lin} at high wavenumbers.

For the narrowband initial conditions this is not such a great concern, as it is relatively easy to specify the standard deviation of the perturbation. As the range of modes is short, this ensures that the root-mean-square amplitude of the mode at the given wavenumber is approximately σ.

For the broadband case, it was decided that the best approach was to fix the level of nonlinearity of the highest wavenumber mode initialized on a given grid. This means that the sequence of simulations on successively finer grids will have the same high wavenumber content; however, each successive refinement will allow a greater range – i.e. extending the power spectrum to lower effective wavenumbers. In this way, it is ensured that the initial perturbation remains linear throughout the grid-refinement study.

This approach is now detailed for the broadband case where $m = -2$. The amplitude of a given mode can be computed from (A 7) as $a_k = 2\sqrt{C/k}$. Assuming that the maximum wavenumber is just linear ($k_{max}a_k = 1/2$), then $Ck_{max} = 1/16$. Using this, the standard deviation σ can be rewritten, noting that $k_{max} = 2\pi/\lambda_{min}$, as

$$\sigma = \frac{1}{8\pi}\sqrt{R-1}\lambda_{min} \approx 0.04\sqrt{R-1}\lambda_{min}. \quad \text{(A 8)}$$

This constrains the maximum standard deviation based on the minimum wavelength initialized. For the simulations within this paper the standard deviation was chosen as

$$\sigma = 0.031\sqrt{R-1}\lambda_{min}, \tag{A 9}$$

which is equivalent to an amplitude of $0.2\lambda_{min}$ where $R = 42.7$. This refers to a simulation of 1024 cells $\lambda_{min} = 8\Delta x$ and $\lambda_{max} = L/3$. This specifies directly the relationship between the range of initialized wavenumbers and the standard deviation.

To maintain a consistent representation of the highest wavenumbers, it is important to fix the power in each individual Fourier mode at the high wavenumbers instead of fixing the root-mean-square amplitude of the perturbation. This means that there will be some slight statistical variation of the standard deviation, which however will not be apparent until late times. As the object of this initial condition is to examine the early time development of the mixing layer, it is more important to fix the amplitude of the high wavenumbers.

A.3. *Linear amplitudes*

Equation (A 6) for the Fourier coefficients can now be rewritten using (A 8) as

$$\sigma_{m,n} = \frac{4\pi\sigma}{L}\left(\frac{k_{max}}{2\pi(R-1)k_{m,n}^3}\right)^{1/2}, \tag{A 10}$$

where $\sigma_{m,n}$ is the standard deviation of the mode with wavenumbers m in the y-direction and n in the z-direction. It now remains to choose a standard deviation for which the amplitude of the highest frequency mode excited remains linear. The required σ to satisfy this constraint is defined in (A 9), giving

$$\sigma_{m,n} = 0.031\frac{4\pi}{L}\left(\frac{\lambda_{min}}{k_{m,n}^3}\right)^{1/2}. \tag{A 11}$$

Given the above result, each simulation is conducted with a fixed domain width and keeping the minimum wavelength a constant multiple of the cell size. Thus, the standard deviation determined *via* (A 11) varies inversely proportional to the square of the grid resolution.

Now (A 11) must be modified to compensate for the doubling of contributions from the zeroth wavenumber (as the summation is computed for one of the four quadrants). Each coefficient is calculated as follows, using $a_{m,n}$ as an example:

$$a_{m,n} = \mathscr{R}S(m)S(n)\sigma_{m,n}, \tag{A 12}$$

where $S(p) = 1/\sqrt{2}$ if $p = 0$, 1 if $p > 0$ and $\mathscr{R}$ is a random number picked from a Gaussian distribution. In most simulations the amplitude of the perturbation is at subgrid scale. To achieve a reasonable representation of the initialized perturbation, cells located on the interface are initialized as a mixture where the volume fraction of one gas within a cell is computed using a second-order interpolation of the perturbation position at the cell faces.

Appendix B. Equivalent velocity perturbation

Considering a single mode from the perturbation detailed in (A 5), the velocity potential is given by

$$\phi_{vel}(x, y, z) = S(x)\phi_0 \exp(-k|x|) \times \left[a\cos(k_y y)\cos(k_z z) + b\cos(k_y y)\sin(k_z z) + c\sin(k_y y)\cos(k_z z) + d\sin(k_y y)\sin(k_z z)\right]. \quad \text{(B 1)}$$

$$S(x) = \begin{cases} 1, & \text{if } h > 0, \\ -1, & \text{if } h < 0, \end{cases} \quad \text{(B 2)}$$

where the initial location of the mixing layer is at $x = 0$, where x is in the direction of shock propagation, y and z range from 0 to L, and ϕ_0 is a parameter that controls the magnitude of the perturbation. For RM, the magnitude of the initial perturbation is determined from linear theory, giving $\phi_0 = At^+\Delta u$. To ensure an initially divergence-free velocity field, a vector potential $\boldsymbol{A}$ is defined such that $\boldsymbol{u} = \nabla \times \boldsymbol{A}$ giving

$$u = -\frac{\partial \phi_{vel}}{\partial x} = \frac{\partial A_z}{\partial y} - \frac{\partial A_y}{\partial z}, \quad v = -\frac{\partial \phi_{vel}}{\partial y} = -\frac{\partial A_z}{\partial x}, \quad w = -\frac{\partial \phi_{vel}}{\partial z} = \frac{\partial A_y}{\partial x}, \quad \text{(B 3)}$$

where the x-component of the vector potential can be neglected as the vector potential is always normal to the x-axis. The components of the vector potential are therefore given by

$$A_y = -\frac{\partial \Phi}{\partial z}, \quad A_z = \frac{\partial \Phi}{\partial y}, \quad \text{where} \quad \Phi = \int \phi \, \mathrm{d}x = -\frac{\phi_0}{k} a_0 \exp[\mathrm{i}(k_y y + k_z z)] \exp(-k|x|), \quad \text{(B 4)}$$

hence

$$A_y(x, y, z) = \phi_0 \exp(-k|x - x_1|)\frac{k_z}{k}[b\cos(k_y y)\cos(k_z z) - a\cos(k_y y)\sin(k_z z) + d\sin(k_y y)\cos(k_z z) - c\sin(k_y y)\sin(k_z z)], \quad \text{(B 5)}$$

$$A_z(x, y, z) = \phi_0 \exp(-k|x - x_1|)\frac{k_y}{k}[-c\cos(k_y y)\cos(k_z z) - d\cos(k_y y)\sin(k_z z) + a\sin(k_y y)\cos(k_z z) + b\sin(k_y y)\sin(k_z z)], \quad \text{(B 6)}$$

where the velocity perturbations decay exponentially away from the interface in agreement with incompressible theory (an approximation to the compressible theory where the decay is slower, Fraley 1986). To compensate for the finite length of the domain, an additional correction factor is added to ensure that the velocities become zero at the boundaries of the domain. The above components of the vector potential are multiplied by

$$\frac{1 - \exp(-2k(h_1 + x))}{1 - \exp(-2kh_1)} \quad \text{if} \quad x < 0, \quad \frac{1 - \exp(-2k(h_2 - x))}{1 - \exp(-2kh_2)} \quad \text{if} \quad x > 0, \quad \text{(B 7)}$$

where h_1 and h_2 are the lengths of the flow domain on the heavy fluid side ($x < 0$) and light fluid side ($x > 0$), respectively. To initialize the flow field, the vector potentials are calculated at the cell centres, then differentiated numerically to gain the velocities at the cell vertices, ensuring that the initial condition is divergence free for the numerical approximation used in TURMOIL3D.

The coefficients a–d are defined as described in (A 12); however, the amplitudes of the modes are reduced to account for the compression of the interface by the passage of the shock wave, using the mean compression rate defined in (2.2). This introduces a

level of uncertainty into the comparison between simulations initialized with velocity or surface perturbations; the quantitative correspondence between the two depends on this scaling factor.

REFERENCES

Almgren, A. S., Bell, J. B., Rendleman, C. A. & Zingale, M. 2006 Low Mach number modelling of type Ia supernovae. Part I. Hydrodynamics. *Astrophys. J.* **637**, 922–936.

Amendt, P., Colvin, J. D., Tipton, R. E., Hinkel, D. E., Edwards, M. J., Landen, O. L., Ramshaw, J. D., Suter, L. J., Varnum, W. S. & Watt, R. G. 2002 Indirect-drive noncryogenic double-shell ignition targets for the National Ignition Facility: design and analysis. *Phys. Plasmas* **9** (5), 2221–2233.

Barenblatt, G. I., Looss, G. & Joseph, D. D. 1983 *Nonlinear Dynamics and Turbulence*. Pitman Publishing.

Barnes, C. W., Batha, S. H., Dunne, A. M., Magelssen, G. R., Rothman, S., Day, R. D., Elliott, N. E., Haynes, D. A., Holmes, R. L., Scott, J. M., Tubbs, D. L., Youngs, D. L., Boehly, T. R. & Jaanimagi, P. 2002 Observation of mix in a compressible plasma in a convergent cylindrical geometry. *Phys. Plasmas* **9** (11), 4431–4438.

Bogey, C., de Cacqueray, N. & Bailly, C. 2009 A shock-capturing methodology based on adaptative spatial filtering for high-order nonlinear computations. *J. Comput. Phys.* **228**, 1447–1465.

Chapman, P. R. & Jacobs, J. W. 2006 Experiments on the three-dimensional incompressible Richtmyer–Meshkov instability. *Phys. Fluids* **18**, 074101.

Clark, T. T. & Zhou, Y. 2006 Growth rate exponents of Richtmyer–Meshkov mixing layers. *J. Appl. Mech.* **73**, 461–268.

Cohen, R. H., Dannevik, W. P., Dimits, A. M., Eliason, D. E., Mirin, A. A., Zhou, Y., Porter, D. H. & Woodward, P. R. 2002 Three-dimensional simulation of a Richtmyer–Meshkov instability with a two-scale initial perturbation. *Phys. Fluids* **14** (10), 3692–3709.

Collins, B. D. & Jacobs, J. W. 2002 PLIF flow visualization and measurements of the Richtmyer–Meshkov instability of an air/SF_6 interface. *J. Fluid. Mech.* **464**, 113–136.

Cook, A. W., Cabot, W. & Miller, P. L. 2004 The mixing transition in Rayleigh–Taylor instability. *J. Fluid Mech.* **511**, 333–362.

Cook, A. W. & Zhou, Y. 2002 Energy transfer in Rayleigh–Taylor instability. *Phys. Rev.* E **66**, 026312.

Dahlburg, J. P., Fyfe, D. E., Gardner, J. H., Haan, S. W., Bodner, S. E. & Doolen, G. D. 1995 Three-dimensional multimode simulations of the ablative Rayleigh–Taylor instability. *Phys. Plasmas* **2** (6), 2453–2472.

Debar, R. 1974 A method in 2-D Eulerian hydrodynamics. *Tech. Rep.* UCID-196831. Lawrence Livermore National Laboratory.

Dimonte, G., Frerking, C. E. & Schneider, M. 1995 Richtmyer–Meshkov instability in the turbulent regime. *Phys. Rev. Lett.* **74**, 4855–4858.

Dimonte, G. & Schneider, M. 1997 Turbulent Richtmyer–Meshkov instability experiments with strong radiatively driven shocks. *Phys. Plasmas* **4** (12), 4347–4357.

Dimonte, G. & Schneider, M. 2000 Density ratio dependence of Rayleigh–Taylor mixing for sustained and impulsive acceleration histories. *Phys. Fluids* **12**, 304–321.

Dimonte, G., Youngs, D. L., Dimits, A., Wunsch, S., Garasi, C., Andrews, M. J., Calder, A. C., MacNeice, P., Ricker, P., Weber, S., Marinak, M., Robinson, A., Ramaprabhu, P., Fryxell, B., Olson, K., Rosner, R., Biello, J., Dursi, L., Timmes, F., Tufo, H., Young, Y.-N. & Zingale, M. 2004 A comparative study of the turbulent Rayleigh–Taylor instability using high resolution three-dimensional numerical simulations: the alpha-group collaboration. *Phys. Fluids* **16** (5), 1668–1693.

Drazin, P. G. & Reid, W. H. 2004 *Hydrodynamic Stability*. Cambridge University Press.

Drikakis, D. 2003 Advances in turbulent flow computations using high-resolution methods. *Prog. Aerosp. Sci.* **39**, 405–424.

Drikakis, D., Hahn, M., Mosedale, A. & Thornber, B. 2009 Large eddy simulation using high-resolution and high-order methods. *Phil. Trans. R. Soc.* A **367** (1899), 2985–2997.

Drikakis, D. & Rider, W. 2004 *High-Resolution Methods for Incompressible and Low-Speed Flows*. Springer.

Drikakis, D. & Tsangaris, S. 1993 On the solution of the compressible Navier–Stokes equations using improved flux vector splitting methods. *Appl. Math. Model.* **17** (6), 282.

Fraley, G. 1986 Rayleigh–Taylor stability for a normal shock wave–density discontinuity interaction. *Phys. Fluids* **29**, 376–386.

Gauthier, S. & Bonnet, M. 1990 A $k-\epsilon$ model for turbulent mixing in shock-tube flows induced by Rayleigh–Taylor instability. *Phys. Fluids* A **2** (9), 1685–1694.

Godunov, S. K. 1959 A finite-difference method for the computation of discontinuous solutions of the equations of fluid dynamics. *Mat. Sb.* **47**, 271–295.

Goncharov, V. N. 2002 Analytical model of nonlinear, single-mode, classical Rayleigh–Taylor instability at arbitrary Atwood numbers. *Phys. Rev. Lett.* **88** (13), 134502.

Grinstein, F. F., Margolin, L. G. & Rider, W. J. (Ed.) 2007 *Implicit Large Eddy Simulation: Computing Turbulent Fluid Dynamics*. Cambridge University Press.

Hill, D. J., Pantano, C. & Pullin, D. I. 2006 Large-eddy simulation and multi-scale modelling of a Richtmyer–Meshkov instability with reshock. *J. Fluid. Mech* **557**, 29–61.

Holmes, R. L., Dimonte, G., Fryxell, B., Gittings, M. L., Grove, J. W., Schneider, M. S., Sharp, D. H., Velikovich, A. L., Weaver, R. P. & Zhang, Q. 1999 Richtmyer–Meshkov instability growth: experiment, simulation and theory. *J. Fluid Mech.* **389**, 55–79.

Huang, M.-J. & Leonard, A. 1994 Power-law decay of homogeneous turbulence at low Reynolds numbers. *Phys. Fluids* **6** (11), 3765–3775.

Inogamov, N. A. 1999 The role of Rayleigh–Taylor and Richtmyer–Meshkov instabilities in astrophysics: an introduction. *Astrophys. Space Phys.* **10**, 1–335.

Inogamov, N. 2006 Richtmyer–Meshkov turbulence. In *Proceedings of the International Workshop on the Physics of Compressible Turbulent Mixing 10*. Available online at: http://www.iwpctm.org/.

Jeong, J. & Hussain, F. 1995 On the identification of a vortex. *J. Fluid. Mech.* **285**, 69–94.

Kim, K. H. & Kim, C. 2005 Accurate, efficient and monotonic numerical methods for multi-dimensional compressible flows. Part II. Multi-dimensional limiting process. *J. Comput. Phys.* **208**, 570–615.

Kolmogorov, A. N. 1941 The local structure of turbulence in an incompressible fluid at very high Reynolds numbers. *Dokl. Akad. Nauk. SSSR* **30**, 299.

van Leer, B. 1977 Towards the ultimate conservative difference scheme. Part IV. A new approach to numerical convection. *J. Comput. Phys.* **23**, 276–299.

Lesieur, M. & Metais, O. 1996 New trends in large-eddy simulations of turbulence. *Annu. Rev. Fluid Mech.* **28**, 45–82.

Llor, A. 2006 Invariants of free turbulent decay. arXiv:physics/0612220v1.

Meshkov, E. E. 1969 Instability of the interface of two gases accelerated by a shock wave. *Fluid Dyn.* **43** (5), 101–104.

Mikaelian, K. O. 1989 Turbulent mixing generated by Rayleigh–Taylor and Richtmyer–Meshkov instabilities. *Physica* D **36**, 343–357.

Mosedale, A. & Drikakis, D. 2007 Assessment of very high-order of accuracy in LES models. *J. Fluids Engng* **129**, 1497–1503.

Oron, D., Arazi, L., Kartoon, D., Rikanati, A., Alon, U. & Shvarts, D. 2001 Dimensionality dependence of the Rayleigh–Taylor and Richtmyer–Meshkov instability late-time scaling laws. *Phys. Plasmas* **8** (6), 2883–2889.

Pope, S. B. 2000 *Turbulent Flows*. Cambridge University Press.

Poujade, O. & Peybernes, M. 2010 Growth rate of Rayleigh–Taylor turbulent mixing layers from first principles. *Phys. Rev. E* **81** (1), 016316.

Prasad, J. K., Rasheed, A., Kumar, S. & Sturtevant, B. 2000 The late-time development of the Richtmyer–Meshkov instability. *Phys. Fluids* **12** (8), 2108–2115.

Ramaprabu, P. K. 2003 On the dynamics of Rayleigh–Taylor mixing. PhD thesis, Texas A&M University.

Ramshaw, J. D. 1998 Simple model for linear and nonlinear mixing at unstable fluid interfaces with variable acceleration. *Phys. Rev.* E **58** (5), 5834–5840.

Richtmyer, R. D. 1960 Taylor instability in shock acceleration of compressible fluids. *Comm. Pure Appl. Math.* **13**, 297–319.

Spiteri, R. J. & Ruuth, S. J. 2002 A class of optimal high-order strong-stability preserving time discretization methods. *SIAM J. Numer. Anal.* **40** (2), 469–491.

Thornber, B. & Drikakis, D. 2007 Large-eddy simulation of multi-component compressible turbulent flows using high resolution methods. *Comput. Fluids* doi:10.1016/j.compfluid.2007.04.009.

Thornber, B. & Drikakis, D. 2008 Implicit large eddy simulation of a deep cavity using high resolution methods. *AIAA J.* **46** (10), 2634–2645.

Thornber, B., Mosedale, A. & Drikakis, D. 2007 On the implicit large eddy simulation of homogeneous decaying turbulence. *J. Comput. Phys.* **226**, 1902–1929.

Thornber, B., Mosedale, A., Drikakis, D., Youngs, D. & Williams, R. 2008 An improved reconstruction method for compressible flows with low Mach number features. *J. Comput. Phys.* **227**, 4873–4894.

Toro, E. F. 1997 *Riemann Solvers and Numerical Methods for Fluid Dynamics*. Springer.

Vincent, A. & Meneguzzi, M. 1991 The spatial structure and statistical properties of homogeneous turbulence. *J. Fluid Mech.* **225**, 1–20.

Youngs, D. L. 1982 Time-dependent multimaterial flow with large fluid distortion. In *Numerical Methods for Fluid Dynamics*, pp. 273–285. Academic Press.

Youngs, D. L. 1991 Three-dimensional numerical simulation of turbulent mixing by Rayleigh–Taylor instability. *Phys. Fluids* A **3** (5), 1312–1320.

Youngs, D. L. 1994 Numerical simulation of mixing by Rayleigh–Taylor and Richtmyer–Meshkov instabilities. *Laser Part. Beams* **12**, 725–750.

Youngs, D. L. 2003 Application of MILES to Rayleigh–Taylor and Richtmyer–Meshkov mixing. *Paper 2003-4102*. AIAA.

Youngs, D. L. 2004 Effect of initial conditions on self-similar turbulent mixing. In *Proceedings of the International Workshop on the Physics of Compressible Turbulent Mixing 9*. Available online at: http://www.iwpctm.org/.

Zhang, Q. & Sohn, S.-I. 1997 Nonlinear theory of unstable fluid mixing driven by shock wave. *Phys. Fluids* **9** (4), 1106–1124.

Zhou, Y. 2001 A scaling analysis of turbulent flows driven by Rayleigh–Taylor and Richtmyer–Meshkov instabilities. *Phys. Fluids* **13** (2), 538–543.